

# CHEMISTRY

## A European Journal

A Journal of



### Accepted Article

**Title:** Development of Polar Order by Liquid Crystal Self-assembly of Weakly Bent Molecules

**Authors:** Mohamed Alaasar, Marko Prehm, Silvio Poppe, and Carsten Tschierske

This manuscript has been accepted after peer review and appears as an Accepted Article online prior to editing, proofing, and formal publication of the final Version of Record (VoR). This work is currently citable by using the Digital Object Identifier (DOI) given below. The VoR will be published online in Early View as soon as possible and may be different to this Accepted Article as a result of editing. Readers should obtain the VoR from the journal website shown below when it is published to ensure accuracy of information. The authors are responsible for the content of this Accepted Article.

**To be cited as:** *Chem. Eur. J.* 10.1002/chem.201606035

**Link to VoR:** <http://dx.doi.org/10.1002/chem.201606035>

Supported by  
**ACES**

WILEY-VCH

# Development of Polar Order by Liquid Crystal Self-assembly of Weakly Bent Molecules

Mohamed Alaasar,<sup>[a,b]\*</sup> Marko Prehm,<sup>[a]</sup> Silvio Poppe,<sup>[a]</sup> Carsten Tschierske<sup>[a]\*</sup>

<sup>[a]</sup> Dr. Mohamed Alaasar, Dr. Marko Prehm, Silvio Poppe and Prof. Dr. Carsten Tschierske  
Institute of Chemistry,  
Martin Luther University Halle-Wittenberg,  
Kurt Mothes Str. 2, D-06120 Halle (Saale), Germany;  
carsten.tschierske@chemie.uni-halle.de

<sup>[b]</sup> Dr. Mohamed Alaasar,  
Department of Chemistry,  
Faculty of Science,  
Cairo University, Giza, Egypt;  
malaasar@sci.cu.edu.eg

**Abstract:** Organic ferroelectrics are of growing importance for multifunctional materials. Here we provide an understanding of the distinct stages of the development of sterically induced polar order in liquid crystalline (LC) soft matter. Three series of weakly bent molecules derived from 4-cyanoresorcinol as the bent core unit with laterally fluorinated azobenzene wings have been synthesized and the effects of the position of fluorine substitution, alkyl chain length and temperature on the LC self-assembly and polar order were studied. In their LC phases a paraelectric-ferroelectric transition takes place by gradual increase of the size of polar domains and by crossing a permittivity maximum, similar to inorganic solid state ferroelectrics. Increasing polar coherence length simultaneously leads to a transition from synpolar to antipolar domain correlation in the high permittivity paraelectric range. Associated with the emergence of polar order is the development of a tilted organization of the molecules and a growing coherence of tilt. This leads to a transition from non-tilted via tilt randomized uniaxial to long range tilted biaxial smectic phases, to surface-stabilized symmetry breaking with formation of chiral conglomerates and field-induced tilt. Moreover, there is a remarkably strong effect of the position of fluorination; polar order is favored by peripheral core substitution and it is suppressed by inside directed fluorination.

## 1. Introduction

Organic compounds with extended aromatic building blocks receive growing importance as charge carrier and optical materials. The majority of these materials are composed of a functional  $\pi$ -conjugated core unit and flexible chains providing processibility due to reduced melting points and increased solubilities, while retaining the organization of the functional units.<sup>[1]</sup> However, the alkyl chains also have an active function as they can modify the mode of self assembly and thus can lead to the emergence of new properties and functionalities. In the ideal case this gives rise to the liquid crystalline (LC) state, intrinsically combining long range order with mobility. In these LC phases the organization of the aromatic cores can be addressed, by different kinds of external stimuli.<sup>[2]</sup> Liquid crystals (LCs) are nowadays considered as a fourth state of matter providing a wide range of soft functional materials<sup>[3]</sup> for numerous application in our daily life, such as liquid-crystal displays (LCDs), adjustable optical elements, tunable lasers, semiconducting layers in organic field effect transistors,<sup>[4]</sup> light emitting diodes, photovoltaic cells and photo-recording devices,<sup>[5,6]</sup> thus making them to that supramolecular systems with the largest impact on the global economies.<sup>[7]</sup> In the wider field of materials, the organic ferroelectrics,<sup>[8]</sup> especially those with LC properties<sup>[9,10]</sup> arose significant interest and the discovery of ferroelectricity, antiferroelectricity and spontaneous mirror symmetry breaking in bent-core liquid crystals (BCLCs) breathed a new area in the field of LCs.<sup>[11-13]</sup> In these ferroelectric and antiferroelectric materials polar order is due to the restricted rotation of BCLCs around their long axis (Scheme. 1a). However, as in these materials the polar order is often combined with a tilt of the molecules with respect to the layer normal, the symmetry is reduced to  $C_2$  leading to superstructural layer chirality (Scheme 1b).<sup>[13,14]</sup> Previous research in this field was predominately focused on high polarization ferroelectric and antiferroelectric bent-core molecules with a bending angle  $\gamma \sim 120^\circ$  (Scheme 1c).<sup>[12,13]</sup> However, also high permittivity paraelectrics and related materials with medium range polar order are of significant interest for super-capacitors and other applications.<sup>15</sup> Therefore, molecules at the cross over between rod-like ( $\gamma \sim 180^\circ$ ) and bent shapes ( $\gamma \sim 120^\circ$ ),<sup>[16-20]</sup> hockey stick molecules, having the bend shifted to one end<sup>[21-24]</sup> and molecules with comparatively short bent-core units.<sup>[25,26]</sup> receive growing interest.

The aim of this article is to provide an understanding of the development of polar order in lamellar liquid crystalline phases at the cross-over from rod-like to bent molecular shapes

depending on alkyl chain length, temperature and position of core fluorination. To this end we have synthesized and investigated a series of new bent-core molecules based on a central 4-cyanoresorcinol core with fluorinated rod-like azobenzene side groups (Scheme 1c).

<Scheme 1>

The 4-cyanoresorcinol bisbenzoate core unit<sup>[27,28]</sup> was chosen because of its comparatively weak and temperature dependent molecular bend, ( $\gamma \sim 130\text{-}145^\circ$ ) arising from the effects of the CN group on the conformation of the adjacent ester group.<sup>[16,27a,29,32a,b]</sup> Azobenzenes were used as peripheral units for their capability of light-induced *trans*-*cis* isomerisation which is of interest for potential application of the compounds as multifunctional photochromic and photoisomerizable materials.<sup>[30-32]</sup> Due to the unique combination of high polarity and low polarizability, as well as steric and conformational effects<sup>33</sup> fluorination of the aromatic core is a powerful tool for tailoring rod-like LC materials for modern LC technologies<sup>[34-35]</sup> and bent-core mesogens for new applications.<sup>[13,16,36,37]</sup> Fluorine substitution of the weakly bent mesogens **Hn**<sup>32</sup> in the peripheral 3-positions, adjacent to the terminal alkoxy chains, leads to the new series of compounds **3Fn** ( $n = 4\text{-}20$ , even numbered chains) reported herein (Scheme 1c). Only compound **3F20** with the longest chains has been described previously.<sup>[37]</sup> The investigation of the chain length and temperature dependent development of distinct LC phase structures and polar order in the complete series **3Fn** is reported herein, which provides new phases and phase sequences and leads to the universal phase diagram shown in Figure 1a, revealing a gradual development of polar order via low and high permittivity paraelectric phases with increasing size of ferroelectric domains (Figure 1b). Shifting the position of fluorine from the peripheral 3-positions to the inner 2-positions (compounds **3Fn** with  $n = 8\text{-}16$ ) or adding F-substituents to the 2-positions (compounds **23Fn** with  $n = 8\text{-}16$ ) removes polar order. Replacing the fluorine in **3F18** by the larger bromine reduces polar order, which is completely removed if it is replaced by the non-polar methyl group. These investigations allow a general understanding of the development of polar order in soft matter and the unusual phenomena associated with the formation and growth of polar domains, as for example, spontaneous mirror symmetry breaking and electric field induced tilt by a non-classical electroclinic effect, and the relations of these phenomena to the molecular structure.

## 2. Results and Discussion

### 2.1 Synthesis

<Scheme 2>

The synthesis of the new fluorinated compounds **3Fn** ( $n = 4-18$ ), **2Fn** and **23Fn** and the related brominated and methylated compounds **Br18** and **Me18**, respectively, was performed as shown in Scheme 2. The target materials were obtained by acylation of 4-cyanoresorcinol (**5**) with two equivalents of the appropriate azobenzene-based benzoyl chloride **4an-4en**.<sup>[38]</sup> All acylation reactions were carried out in the presence of triethylamine as base and pyridine as acylation catalyst.<sup>[37]</sup> The benzoic acids **3an-3en** were synthesized in a coupling reaction between substituted phenols and the diazonium salt of ethyl 4-aminobenzoate affording the azobenzenes (**1a-e**) in a first step. This was followed by etherification of **1a-e** with different 1-bromoalkanes to give the ester compounds **2an-2en**, which were then hydrolysed under basic conditions yielding the desired acids **3an-3en**.<sup>[38]</sup>

### 2.2 Development of tilt and polar order in the LC phases of 3-fluorinated compounds (3Fn)

<Table 1, Figure 1>

The phase sequences, transition temperatures and the associated transition enthalpies of the series of even numbered homologous of compounds **3Fn** ( $n = 4 - 20$ ) are collated in Table 1 and shown graphically in Figure 1a. The phase abbreviations are explained in Table 1 and Figure 1b and will be elaborated in the course of this section. In brief, SmA and SmC designate lamellar phases with non-tiled or tilted organization of the molecules in the layers, respectively, the suffixes P<sub>R</sub> and P<sub>AR</sub> indicate high permittivity paraelectric phases composed of ferroelectric domains, P<sub>A</sub> indicates antiferroelectric LC phases with macroscopic polar order and [\*] indicates the formation of chiral conglomerates in the corresponding phases (see Section 3.1.5).

As schematically shown in Figure 1 all compounds **3Fn** with  $n = 12-20$  exhibit a uniaxial SmA phase range at high temperature followed on cooling by biaxial LC phases representing tilted paraelectric (SmC<sub>s</sub>[\*], SmC<sub>s</sub>P<sub>R</sub>[\*], SmC<sub>s</sub>P<sub>AR</sub>) and polar (SmC<sub>s</sub>P<sub>A</sub>, SmC<sub>a</sub>P<sub>A</sub>) smectic phases (Table 1). In the LC temperature range only the SmA-SmC and the paraelectric-antiferroelectric transitions are associated with enthalpy changes, whereas the other transitions are continuous. For

the short chain compounds ( $n = 4-10$ ) other phase sequences were observed. Thus, for chain lengths  $n = 6-10$  uniaxial high permittivity paraelectric smectic phases ( $\text{SmAP}_R$  and  $\text{SmAP}_{AR}$ ) develop, while compounds with  $n = 4$  and 6 form cybotactic nematic phases ( $\text{N}_{\text{CybA}}$ ). In the following, the development of the distinct LC phases will be discussed step-by-step, starting with the nematic phases. In Sections 2.3 and 2.4 the series  $\mathbf{3Fn}$  will be compared with related compounds and the effects of changing the position of fluorination will be discussed.

### 2.2.1 Compounds $\mathbf{3F4}$ and $\mathbf{3F6}$ and the non-skewed cybotactic nematic phases

The shortest homologue of the series  $\mathbf{3Fn}$  with  $n = 4$  forms a monotropic (metastable) nematic phase at  $T = 136$  °C which rapidly crystallizes at  $T = 97$  °C, whereas the nematic phase of the next higher homologue  $\mathbf{3F6}$  is enantiotropic. The XRD pattern of an oriented sample of the nematic phase of  $\mathbf{3F6}$  in a magnetic field ( $B \approx 1$  T, see Figure 2a,b) shows a diffuse scattering with a maximum at  $d = 0.45$  nm located on the equator and a diffuse scattering with a single maximum at  $d = 3.88$  nm on the meridian, being slightly shorter than the molecular length  $L_{\text{mol}} = 4.4$  nm (determined for an assumed  $\Lambda$ -shaped conformation with  $120^\circ$  bending angle and stretched *all-trans* alkyl chains, see Figure S9). This diffraction pattern indicates a nematic phase composed of cybotactic clusters with local SmA structure ( $\text{N}_{\text{CybA}}$ )<sup>[39,40]</sup> which is rarely observed for bent-core mesogens, usually preferring tilted arrangements.<sup>[28]</sup>

<Figure 2>

### 2.2.2 Uniaxial SmA and $\text{SmAP}_R$ phases

At  $T = 110$  °C the diffuse scattering in the small angle region of the diffraction pattern of  $\mathbf{3F6}$  transforms into a sharp Bragg peak with  $d = 4.0$  nm as typical for a transition to a smectic phase (Figure 2c, d). The maximum of the diffuse scattering in the wide angle region remains perpendicular to the small angle reflection, indicating an on average non-tilted organization of the molecules in the layers. The  $d$ -spacing in this SmA phase is only a bit smaller than the molecular length ( $d/L_{\text{mol}} = 0.91$  nm), in line with a monolayer SmA structure. This phase assignment is in agreement with optical investigations between crossed polarizers, indicating typical fan textures in planar alignment (molecules parallel to the surfaces) with dark extinction crosses being parallel to the directions of polarizer and analyzer (see inset in Figure 2c and Figure S7b). In homeotropic

cells (layers parallel to the surfaces) the textures appear completely dark between crossed polarizers, i.e. this phase is optically uniaxial as typical for the SmA phase. SmA phases are formed by all compounds **3F $n$**  with  $n \geq 8$ , being the first LC phase observed on cooling from the isotropic liquid state (Table 1, Figure 1a).

<Figure 3>

As shown in the plots in Figure 3, in the high temperature range of all SmA phases (including those designated as SmAP<sub>R</sub>) an increase of the layer spacing  $d$  is observed on cooling, which is due to an increasing packing density of the aromatic cores with decreasing temperature. The denser packing leads to an alkyl chain stretching and this increases the layer spacing  $d$ . However, the slope of the  $d = f(T)$  function decreases until a maximum is reached and then  $d$  decreases on further cooling. The decrease of  $d$  starts already in the temperature range of the uniaxial SmA phase and therefore is attributed to a developing tilt with formation of randomly aligned tilt domains (de Vries-like smectic phase<sup>[41]</sup>) and partially also to a reduction of the effective molecular length by decrease of the angle  $\gamma$  between the two rod-like azobenzene units (Figure 1c), thus favouring the development of polar domains. On further cooling the formation of tilted smectic phases (SmC) is observed for all compounds with  $n > 4$ , which is in line with the proposed contribution of tilt to the layer shrinkage. With growing alkyl chain length ( $n$ ) the SmC range broadens and the temperature range of the SmA phase becomes smaller and it is shifted to higher temperatures till  $n = 16$ , but even for the longest homologues ( $n = 18, 20$ ) a small range of the SmA phase is retained (Figure 1a). The response of the SmA phases to an applied electric field changes with chain length, applied field strength and temperature. The remarkable feature of the short chain compounds **3F6**, **3F8** and **3F10** is, that in the whole SmA range a relatively broad single current peak is reproducibly observed in each half period of an applied triangular wave field (Figures 4a and S13). This peak is thought to be the result of a Langevin-type growth and switching of ferroelectric domains under the applied E-field, as known for SmAP<sub>R</sub> phases.<sup>[42,43,44]</sup> The current peak occurs above a certain threshold field which increases with growing chain length. Similarly, under a fixed field strength ( $E = 27 \text{ V}_{pp} \mu\text{m}^{-1}$ ) the temperature of emergence of this peak is continuously shifted to lower temperature with growing chain length (Table 1 and Figure 1a). For compound **3F12** there is no current peak in the SmA range and the emergence of the current peak coincides with the SmA to SmC phase transition (SmA - SmC<sub>s</sub>P<sub>R</sub><sup>[\*]</sup>). For the

following homologues ( $n > 12$ ) the current peak appears only after the SmA-SmC transition within the SmC range, leading to  $\text{SmC}_s^{[*]} - \text{SmC}_s\text{P}_R^{[*]}$  transitions. The single peak switching in the  $\text{SmC}_s\text{P}_R^{[*]}$  ranges is associated with an increase of the birefringence of the planar sample under the applied E-field (Figure S16i-k), confirming that this peak is indeed due to a polarization. The polarization calculated from the peak area is the largest for the  $\text{SmAP}_R$  phase of **3F6** ( $P = \sim 160 \text{ nC cm}^{-2}$ ) and decreases with growing chain length to only  $\sim 50 \text{ nC cm}^{-2}$  in the  $\text{SmC}_s\text{P}_R^{[*]}$  ranges of compounds **3F12-3F18**. No polarization peak can be observed in the SmA phases of the long chain compounds **3F10-3F20**, considered as low permittivity paraelectric SmA phases, in contrast to the  $\text{SmAP}_R$  (and  $\text{SmAP}_{AR}$ ) phases which are considered as high permittivity paraelectric phases.

### 2.2.3 The uniaxial $\text{SmAP}_{AR}$ range of compounds **3F6** and **3F8**

<Figure 4>

Within the uniaxial smectic phases of compounds **3F6** and **3F8** with shortest chains the mode of switching changes below a certain temperature (Figures 4 and S11). For **3F8**, for example, the broad single peak in the  $\text{SmAP}_R$  range (Figure 4a) is replaced by two sharp current peaks per half period of the applied triangular wave voltage at  $T = 108 \text{ }^\circ\text{C}$  and  $20 \text{ V}_{pp}\mu\text{m}^{-1}$  (Figure 4b). These current peaks are positioned at the maximum voltages and merge closer to each other on further cooling (Figure 4c,d). At the transition to this uniaxial SmA phase, designated as  $\text{SmAP}_{AR}$ , (for textures see Figure 4e with inset) the polarization jumps from 150 to  $\sim 700 \text{ nC cm}^{-2}$  and then further grows to  $\sim 800 \text{ nC cm}^{-2}$ , indicating the development of an almost macroscopic polarization under the applied field (Figure 5a). The absence of an enthalpy change at this transition (see Table 1 and Figure S6a) means that despite of the high polarization values this phase range is still paraelectric. Moreover, there is a strong field dependence of the temperature of occurrence of the two switching peaks, being shifted to higher temperature with growing strength of the applied E-field ( $T = 107 \text{ }^\circ\text{C}$  for  $16 \text{ V}_{pp}\mu\text{m}^{-1}$ ,  $110 \text{ }^\circ\text{C}$  for  $27 \text{ V}_{pp}\mu\text{m}^{-1}$  and  $112 \text{ }^\circ\text{C}$  for  $33 \text{ V}_{pp}\mu\text{m}^{-1}$ , see Figure S12). For **3F6** the same behaviour as for **3F8** is found, but the two widely separated current peaks emerge at slightly lower temperature ( $T = 101 \text{ }^\circ\text{C}$  and  $27 \text{ V}_{pp}\mu\text{m}^{-1}$ , see Figure S11).

<Figure 5>

Optical investigations of the SmAP<sub>AR</sub> range indicates a planar fan-texture with dark extinctions parallel to the directions of the polarizers (Figure 6a) which is changed under the applied E-field to a texture composed of dark and bright (orange) areas (Figure 6c). In Figure 6a,c and e the alignment of the layers is slightly inclined with the orientation of the crossed polarizers and rotation of the sample to the opposite direction of inclination exchanges the brightness of the domains. This indicates a field induced uniform (synclinic) tilt, having opposite tilt direction in the distinct areas (Figure 6c,d).

< Figure 6 >

Upon removal of the field the direction of tilt is retained (Figure 6e,f), indicating that the synclinic tilted state is preserved at  $E = 0$ ; thus, we conclude on a uniaxial smectic phase composed of ferroelectric SmC<sub>s</sub>P<sub>S</sub> domains being tilt-randomized in the pristine state (Figure 6a,b). Under an applied field the domains grow and adopt uniform tilt correlation, leading to a field-induced biaxial and synpolar SmC<sub>s</sub>P<sub>S</sub> state (Figure 6c,d) which relaxes to an antipolar SmC<sub>s</sub>P<sub>A</sub> state at  $E = 0$  (Figure 6e,f). This field induced formation of a tilted organization could be considered as a non-classical kind of electroclinic effect,<sup>[45,22]</sup> or alternatively, as a transition to a field induced and surface stabilized state.<sup>[16b,46]</sup> During relaxation and also after field reversal the tilt direction is retained, indicating an antiferroelectric switching by collective rotation around the molecular long axis (Figure 6d,f). This range of the uniaxial SmA phase, representing a lamellar phase composed of tilt randomized SmC<sub>s</sub>P<sub>S</sub> domains and having a dominating antipolar correlation between them in the ground state (Figure 6b), is designated as SmAP<sub>AR</sub>.<sup>[47-49]</sup> At the SmAP<sub>R</sub>-SmAP<sub>AR</sub> transition the preferred mode of correlation between the ferroelectric domains changes from synpolar in SmAP<sub>R</sub> (single current peak) to antipolar in SmAP<sub>AR</sub> (double current peak).

#### 2.2.4 The biaxial SmC<sub>s</sub>P<sub>AR</sub> phase of compound 3F10

For the next homologue **3F10** a birefringent schlieren texture spontaneously occurs at  $T = 112$  °C on cooling the homeotropically aligned uniaxial SmAP<sub>R</sub> phase (Figure S8a). In XRD patterns a decrease of the layer spacing from  $d = 4.6$  nm to 4.3 nm starts at  $\sim 125$  °C in the SmAP<sub>R</sub> phase

and continues in the biaxial phases (Figure 3b), in line with a growing tilt with decreasing temperature. Optical investigations of planar samples confirm a synclinic tilted organization (Figure S15h). At the transition to this biaxial phase two widely separated polarization peaks appear in each half-period of an applied triangular wave field, which rapidly merge closer and increase in size (Figure S14), just as found for the SmAP<sub>AR</sub> phase of **3F8** (Figure 4a-d). In electrooptical investigations the removal of the applied field and inversion of the field direction does not change the tilt direction (see Figure S15g-i), indicating that also in this phase the switching process takes place by rotation around the molecular long axis (Figure S15j-l). This biaxial smectic phase, designated as SmC<sub>s</sub>P<sub>AR</sub>, behaves just like the SmAP<sub>AR</sub> phase of **3F8**. Only the tilt correlation between the SmC<sub>s</sub>P<sub>S</sub> domains is synclinic already before application of an E-field, meaning that elongated alkyl chains favor the long range tilt correlation between the SmC<sub>s</sub>P<sub>S</sub> domains. Similar to the SmAP<sub>AR</sub> range, also in the SmC<sub>s</sub>P<sub>AR</sub> phase the polarization strongly rises from ~50 to ~800 nC cm<sup>-2</sup> (Figure 5b).

### 2.2.5 Development of polar order in the SmC phases of compounds **3F12-2F20**: SmC<sub>s</sub><sup>l</sup>/<sub>s</sub><sup>d</sup>, SmC<sub>s</sub>P<sub>R</sub><sup>l</sup>/<sub>s</sub><sup>d</sup> and SmC<sub>s</sub>P<sub>AR</sub> ranges

<Figure 7>

Whereas for compound **3F10** the phase biaxiality appears to develop simultaneously with the double peak switching at the SmAP<sub>R</sub>-SmC<sub>s</sub>P<sub>AR</sub> transition, for the next homologue **3F12** phase biaxiality already emerges together with the appearance of the single current peak (peak **A** in Figure 7a, see also Figure S13b) at  $T = 135\text{ }^{\circ}\text{C}$  ( $E = 27\text{ V}\mu\text{m}^{-1}$ ), i. e. the SmAP<sub>R</sub> phase is replaced by a SmC<sub>s</sub>P<sub>R</sub> phase with long range tilt.

<Figure 8>

The texture of the homeotropically aligned sample of the SmC<sub>s</sub>P<sub>R</sub> phase of **3F12** before application of an E-field is shown in Figure 8. Between crossed polarizers there are areas with uniformly weak birefringence, being separated by dark domain walls (Figure 8b). After decrossing the polarizers by a small angle of about 5-10° the distinct areas become dark and bright and decrossing the polarizer in the opposite direction reverses the brightness (Figure 8a,c).

Rotation of the sample between crossed polarizers does not change the brightness, meaning that simple tilt domains can be excluded and formation of a conglomerate of optical active domains is observed. This indicates chiral conglomerate formation in these  $\text{SmC}_s\text{P}_R$  phases, which leads to the designation  $\text{SmC}_s\text{P}_R^{[*]}$ , where the star in brackets stands for the conglomerate structure. On cooling, the chiral domains disappear and simultaneously two broad and widely separated polarization peaks develop at  $T = 111\text{ }^\circ\text{C}$  (peaks **B** in Figure 7b-d), just as observed for the  $\text{SmC}_s\text{P}_{AR}$  phase of **3F10**. However, the broad shape of the two emerging polarization peaks in the  $\text{SmC}_s\text{P}_{AR}$  range of compound **3F12** is distinct from the sharp peaks in the  $\text{SmAP}_{AR}$  and  $\text{SmC}_s\text{P}_{AR}$  phases of the shorter homologues **3F8** and **3F10**. Peak broadening increases with growing chain length and is associated with a smoother increase of the polarization in the  $\text{SmC}_s\text{P}_{AR}$  range to only  $\sim 400\text{ nC cm}^{-2}$  (see Figure 5c for **3F12** and Figure 5d for **3F14**). It appears that the lateral expansion of the conformationally disordered alkyl chains reduces the polar packing of the aromatic cores, thus reducing the overall polarity of the domains and requiring larger domain size to achieve the same polarization. Apparently, high polarization density leads to small domains with narrow size distribution, yielding sharp polarization peaks, whereas low polarization density requires larger domains which have a broader size distribution, leading to broader polarization peaks.

For compounds **3Fn** with  $n > 12$  chiral domain formation appears together with the onset of tilt, whereas the emergence of a current peak is delayed and takes place significantly after tilt correlation, i.e. the paraelectric  $\text{SmC}$  phase is divided into a low permittivity chiral  $\text{SmC}_s^{[*]}$  range at highest temperature, followed at lower temperature by chiral and achiral high permittivity  $\text{SmC}_s\text{P}_R^{[*]}$  and  $\text{SmC}_s\text{P}_{AR}$  ranges, respectively. In the planar textures of the  $\text{SmC}_s\text{P}_R^{[*]}$  and  $\text{SmC}_s\text{P}_{AR}$  ranges of all compounds **3Fn** the orientation of the extinction crosses is inclined with the directions of polarizer and analyzer under the  $E$ -field as well as at  $E = 0$  (Figs. 7f-h and j-l and S16i-k and l-n). This confirms a synclinal tilt-correlation and a switching by reorganization of the molecules by a rotation around the molecular long axis (Figure 7i and m). This switching requires a threshold field which decreases with decreasing temperature due to growing polarization and domain size. For a fixed field strength ( $27\text{ V}\mu\text{m}^{-1}$ ) the temperature of appearance of the single polarization peak ( $\text{SmC}_s^{[*]}-\text{SmC}_s\text{P}_R^{[*]}$  transition temperature) decreases with growing chain length and for compound **3F20** with the longest chains the  $\text{SmC}_s\text{P}_R^{[*]}$  range appears to be completely removed and a direct  $\text{SmC}_s^{[*]}-\text{SmC}_s\text{P}_{AR}$  transition, without intermediate  $\text{SmC}_s\text{P}_R^{[*]}$  phase, is observed (Table 1 and Figure 1a).<sup>37</sup> Dielectric studies of this compound<sup>[37]</sup> have

confirmed a continuous increase of the dielectric permittivity in the paraelectric SmC range, reaching a maximum in the SmC<sub>s</sub>P<sub>AR</sub> range just before the transition to the antiferroelectric SmC<sub>s</sub>P<sub>A</sub> phase (Figure 9b),<sup>[50]</sup> in line with previously reported paraelectric-ferroelectric transitions.<sup>[51]</sup> Furthermore, chunks of SmC<sub>s</sub>P<sub>S</sub> domains, being about 10-20 layers thick, have been observed by polarizing microscopy of freely suspended films in the SmC<sub>s</sub>P<sub>AR</sub> range of **3F20**, thus supporting the proposed polar domain structure of the - SmC<sub>s</sub>P<sub>AR</sub> phase.<sup>[37]</sup>

The unique feature of the series of compounds **3Fn** is, that four different types of polarization randomized smectic phases, the uniaxial (SmAP<sub>R</sub>, SmAP<sub>AR</sub>)<sup>[42,47]</sup> and the biaxial (SmC<sub>s</sub>P<sub>R</sub><sup>[\*]</sup> and SmC<sub>s</sub>P<sub>AR</sub>)<sup>[32a,b,37]</sup> were for the first time observed side by side in a single series of compounds which provides insights into the actual structure of these high permittivity paraelectric phases and the relations between them. The broad single peak in the SmAP<sub>R</sub> phases is attributed to a Langevin-type switching.<sup>[42]</sup> However, in the synclinic tilted SmC<sub>s</sub>P<sub>R</sub><sup>[\*]</sup> phases of the higher homologues<sup>[32a,b,37]</sup> tilt and polar order are intrinsically coupled due to the restricted rotation around the molecular long axis and therefore, the polar direction cannot be completely randomized. Due to the uniform tilt there is an Ising-like synpolar coupling between the SmC<sub>s</sub>P<sub>S</sub> domains which supports the formation of synpolar order under the applied field, even if the local polarization is relatively weak. With growing domain size and polarization at reduced temperature a growing preference of antipolar correlation between the SmC<sub>s</sub>P<sub>S</sub> domains develops, leading to a transition to the tristable switching in the SmC<sub>s</sub>P<sub>AR</sub> ranges.

<Figure 9>

Even in the uniaxial SmAP<sub>R</sub> and SmAP<sub>AR</sub> phases with randomized tilt the local tilt could provide cooperativity by Ising-like polar coupling and this could contribute to the polar response in these uniaxial phases.

For all compounds **3Fn** chiral conglomerates appear (Figure 8) just at the onset of phase biaxiality (tilt) at the SmA-SmC<sub>s</sub><sup>[\*]</sup> or SmA-SmC<sub>s</sub>P<sub>R</sub><sup>[\*]</sup> transition and fade upon approaching the SmC<sub>s</sub>P<sub>AR</sub> region which is achiral. Mirror symmetry breaking in synclinic SmC phases of achiral bent-core molecules requires the presence of an intrinsically chiral SmC<sub>s</sub>P<sub>S</sub> structure with C<sub>2</sub> symmetry.<sup>[14]</sup> In the SmC<sup>[\*]</sup> and SmC<sub>s</sub>P<sub>R</sub><sup>[\*]</sup> ranges the Ising-like synpolar coupling between the local SmC<sub>s</sub>P<sub>S</sub> domains and the further stabilization of this coupling by polar surface interactions in the homeotropic cells leads to long range uniform chirality and the emergence of

conglomerates of macroscopically chiral domains (see Figure 8).<sup>[32]</sup> Moreover, the 4-CN group supports twisted minimum energy conformations, thus compounds **3Fn** are considered as transiently chiral molecules favoring chirality synchronization in their smectic phases.<sup>[52,27a,53]</sup> The  $\text{SmC}_s\text{P}_{\text{AR}}$  range with synclinc tilt correlation, but antipolar correlation between adjacent  $\text{SmC}_s\text{P}_s$  domains is on a macroscopic scale racemic and thus achiral. This is in line with a fading of the chiral domains at the transition to  $\text{SmC}_s\text{P}_{\text{AR}}$ .

### 2.2.6 Macroscopic polar $\text{SmC}_s\text{P}_A$ and $\text{SmC}_a\text{P}_A$ phases

For all compounds with  $n > 6$  the further reduction of temperature leads to an increase of the size and polarization of the ferroelectric domains, giving rise to phase transitions to antipolar SmC phases composed of polar layers, associated with a transition enthalpy decreasing with growing alkyl chain length (Table 1). The short chain compounds **3F8** and **3F10** form exclusively anticlinic tilted  $\text{SmC}_a\text{P}_A$  phases on cooling the paraelectric  $\text{SmAP}_{\text{AR}}$  and  $\text{SmC}_s\text{P}_{\text{AR}}$  phases, respectively. In these  $\text{SmC}_a\text{P}_A$  phases antiferroelectric switching takes place with high polarization values and by rotation on the tilt cone as typical for the  $B_2$  phases of bent-core molecules.<sup>[13]</sup> This mode of switching is indicated by the flipping of the dark extinction crosses from being parallel to inclined with the direction of the polarizers either clockwise or anticlockwise, depending on the field direction (Figures 7r-u and S16r-t). The polarization values are high ( $\sim 900 \text{ nC cm}^{-2}$ ) for the short homologues and decrease with growing alkyl chain length to about  $450 \text{ nC cm}^{-2}$  (Figure 9a). For the homologues with  $n \geq 12$  an additional synclinc  $\text{SmC}_s\text{P}_A$  range is introduced between the  $\text{SmC}_s\text{P}_{\text{AR}}$  and the  $\text{SmC}_a\text{P}_A$  phases. The  $\text{SmC}_s\text{P}_A$ - $\text{SmC}_a\text{P}_A$  transition temperature, which is not associated with any transition enthalpy, only slightly decreases with chain elongation from  $T = 98 \text{ }^\circ\text{C}$  for **3F12** to  $T = 92 \text{ }^\circ\text{C}$  for **3F20** (Table 1). The absence of a transition enthalpy confirms that both phases belong to the polar smectic phases with long range polar order in the layers. However, for compounds **3F14-3F20** the switching in the  $\text{SmC}_s\text{P}_A$  phases takes place by rotation around the long axis, as indicated by the fixed position of the dark extinctions with and without applied field (see Figure S16o-q). Only in the  $\text{SmC}_s\text{P}_A$  phase of **3F12**, being the shortest homologue with this phase, the position of the extinctions is retained after switching off the applied field and changes after field reversal (Figure 7n-p). Since there are two polarization peaks (Figure 7d) a bistable switching can be excluded and the actual switching process is interpreted as a combination of two switching mechanisms (see Figure 7q).

A relaxation after switching off the field at 0V taking place by rotation around the long axis, thus retaining the position of the extinctions (Figure 7n,o) and after field reversal a switching by rotation on the tilt cone which rotates the position of the extinctions to the opposite direction (Figure 7o,p), indicating an inversion of the tilt direction.<sup>[54]</sup> In general, high packing density in highly polarized SmC phases of strongly bent molecules suppresses the switching around the long axis whereas low packing density and reduced polar order of weakly bent molecules are favorable for the rotation around the molecular long axis.<sup>[55]</sup> Therefore, it can be deduced that in the SmC<sub>s</sub>P<sub>A</sub> phase the packing density still grows and that a critical limit of packing density and bending angle, changing the tilt correlation and switching mechanism, is achieved at the SmC<sub>s</sub>P<sub>A</sub> to SmC<sub>a</sub>P<sub>A</sub> transition. The SmC<sub>s</sub>P<sub>A</sub> phase of **3F12**, combining both switching mechanisms represents an intermediate case with intermediate packing density. In the SmC<sub>s</sub>P<sub>A</sub> ranges the barrier for the rotation around the molecular long axis is still growing with decreasing temperature, leading to the strong growth of the polarization in the SmC<sub>s</sub>P<sub>A</sub> ranges (Figure 5c,d).

### 2.2.7 Overall phase sequence depending on temperature and chain length

Because the shape of bent molecules based on 4-cyanoresorcinol can change from being almost rod-like to increasingly bent on decreasing temperature,<sup>[27a]</sup> restriction of the rotation around the long axis, increasing packing density and growing coherence length of polar order are observed by reducing the temperature. For only weakly bent molecules there are entropically favored interlayer fluctuations along the molecular long axes, transferring polar order predominately between the layers, whereas the rotation around the long axis reduces polar order in the layers (see Figure 10, left). The weak synpolar coupling in all directions leads to the polarization randomized paraelectric SmAP<sub>R</sub> and SmC<sub>s</sub>P<sub>R</sub><sup>[\*]</sup> phases with a single switching current peak and small polarization values.

<Figure 10>

The transition from a preferred synpolar correlation in SmAP<sub>R</sub>/SmC<sub>s</sub>P<sub>R</sub><sup>[\*]</sup> to the antipolar correlation in the SmAP<sub>AR</sub>/SmC<sub>s</sub>P<sub>AR</sub> phases is thought to be mainly the result of the stronger molecular bend, disfavoring the fluctuations parallel the molecular long axes, but favoring fluctuations by intercalations of the two individual rod-like wings (see Figure 10, right). This

leads to a preference of antipolar coupling, whereas the simultaneous reduction of the ability of rotation around the long axis strengthens the polar coupling in the layers. Thus, two polarization peaks are observed in the paraelectric  $\text{SmAP}_{\text{AR}}$  and  $\text{SmC}_s\text{P}_{\text{AR}}$  phases and the polarization values grow. Further growing in-layer polarization finally leads to polar layers in the antipolar  $\text{SmC}_s\text{P}_A$  and  $\text{SmC}_a\text{P}_A$  phases, resembling the  $B_2$  type polar smectic phase of typical (strongly bent) bent-core mesogens. In the series of compounds  $3\text{Fn}$  growing coherence length of polar order unavoidably leads to antipolar correlation, even before macroscopic polarization is achieved. However, as previously shown, the interlayer fluctuations of the rod-like wings can be suppressed by introduction of nano-segregating silyl groups to the ends of the alky chains<sup>[56,57]</sup> and this shifts the synpolar-antipolar transition into the region of the macroscopic polar smectic phases, thus leading to the ferroelectric switching  $\text{SmC}_s\text{P}_F$ <sup>[58,59]</sup> and  $\text{SmAP}_F$  phases.<sup>[60]</sup>

There is also a significant effect of chain length; short chains ( $n = 4-6$ ) have a small segregation tendency from the aromatic cores<sup>[61]</sup> and this leads to cybotactic nematic phases and  $\text{SmA}$  phases ( $\text{SmAP}_R$ ,  $\text{SmAP}_{\text{AR}}$ ). For medium chain length ( $n = 8-10$ ) core-chain nano-segregation is increased, favouring polar packing in the layers and tilting. Therefore, the medium chain compounds have high polarization values and an increased tendency for antipolar packing in adjacent layers, and this leads to a dominance of the high polarization  $\text{SmC}_a\text{P}_A$  phase. For long chains ( $n = 12-20$ ) the growing mismatch between the cross sectional areas of the rigid aromatic cores and the conformationally disordered flexible chains gives rise to further growing tilt and reduces the packing density, indicated by increasing tilt, reduced polarization and a decreasing temperature range of the  $\text{SmC}_s\text{P}_R$ <sup>[\*]</sup> phase. Simultaneously, with growing chain length the temperature dependent development of the coherence length of polar order becomes more continuous, leading to a growing temperature range of the high permittivity paraelectric  $\text{SmC}_s\text{P}_{\text{AR}}$  region above the paraelectric-antiferroelectric transition and the emergence of an additional synclinc  $\text{SmC}_s\text{P}_A$  range in the antiferroelectric phase region before the transition to the  $B_2$ -like anticlinic  $\text{SmC}_a\text{P}_A$  phase (Figure 1a). In the  $\text{SmC}_s\text{P}_A$  range there is still a growing packing density, which leads to growing polarization; tilt correlation and switching process change at a critical coherence length of polarization at the  $\text{SmC}_s\text{P}_A$ - $\text{SmC}_a\text{P}_A$  transition.

### 2.3 Effects of the replacement of F by H or larger groups in the 3-positions

Comparison of compounds **3Fn** (Figure 1a) with the related non-fluorinated analogues **Hn** (X, Y = H, see Figure 11)<sup>[32a,b]</sup> shows that core fluorination at the periphery leads to an increased stability of smectic phases and shifts the nematic range to much shorter chain length. Moreover, for the fluorinated compounds, there is a reduced tendency to form uniformly tilted phases. Thus, the  $N_{CybC}$  phase of **Hn** is replaced by the  $N_{CybA}$  phase and uniaxial smectic phases ( $SmA$ ,  $SmAP_R$ ,  $SmAP_{AR}$ ) are introduced which are completely missing in the series of the non-fluorinated compounds **Hn**. The stronger tilt in the series **Hn** might also be responsible for the presence of an additional, possibly modulated phase  $M_1$ , separating the paraelectric and antiferroelectric smectic phases. In both series there is mirror symmetry breaking in the  $SmC_s^{[*]}$  and  $SmC_sP_R^{[*]}$  ranges as indicated by surface stabilized conglomerate formation. However, only compounds **3Fn** form the  $B_2$ -like  $SmC_aP_A$  phase with long range polar layers, whereas the paraelectric  $SmC_s^{[*]}$ ,  $SmC_sP_R^{[*]}$  and  $SmC_sP_{AR}$  phases and the  $SmC_sP_A$  phase with limited coherence length of polar order were found in both series. Thus, in the series of the fluorinated compound **3Fn** an increased polar order is achieved. These effects of core fluorination appear to be the result of increased core-core interactions between the electron deficit fluorinated aromatic units.<sup>[62]</sup>

<Figure 11>

Moreover, in the series of compounds **3Fn** and **Hn** there is an opposite effect of increasing chain length on polar order. For compounds **3Fn** the  $SmC_sP_R^{[*]}$  and  $SmC_sP_{AR}$  phases are destabilized with growing chain length whereas for compounds **Hn** these are stabilized (compare Figures 1a and 11). It appears that for compounds **Hn** the weaker core-core interactions are strengthened by increased core-chain nano-segregation, growing with rising chain length. For the fluorinated compounds **3Fn** with stronger core-core interactions core chain segregation is not required. In this case it even disturbs the development of polar order as longer fluid alkyl chains could reduce the packing density of the aromatic cores due to the growing lateral expansion of the disordered alkyl chains.

Replacing fluorine (crystal volume  $cv = 12.8 \text{ nm}^3$ )<sup>[63]</sup> in **3F18** by the more bulky and less polar bromine ( $cv = 33.0 \text{ nm}^3$ ) reduces the phase transition temperatures considerably (compound **3Br18**, Table 2), though a phase sequence Iso- $SmA$ - $SmC_s^{[*]}$ - $SmC_sP_{AR}$  is retained. However, the polarization is smaller ( $P \sim 100 \text{ nC cm}^{-2}$ ) and the polarization peaks are much broader in the  $SmC_sP_{AR}$  range (see Figure S19), indicating a smaller polarization and a significant size

distribution of the polar domains. In this case no transition to a macroscopically polar SmCP<sub>A</sub> phase can be found before crystallization takes place at  $T = 67$  °C. Replacing Br by the non-polar CH<sub>3</sub> group ( $cv = 31.7$  nm<sup>3</sup>) with similar volume further reduces the LC phase stability considerably, removes the non-tilted SmA phase and removes polar order completely, leaving only a nematic (N<sub>Cybc</sub>) and a nonpolar and nonchiral SmC phase (see Table 2). This is mainly attributed to the unfavorable reduction of core-core interactions by the non-polar and electron donating CH<sub>3</sub> group.

<Table 2>

## 2.4 Effects of variation of the F-substitution pattern

<Table 3>

Changing the position of the lateral fluorine substituents from the ortho position (**3Fn**) to the meta position with respect to the terminal alkyloxy chains (**2F**) reduces melting and clearing temperatures (Tables 1 and 3). Moreover, only LC phases with tilted organization (N<sub>Cybc</sub> phases, see Figure S17 and SmC<sub>s</sub> phases) were observed. Neither chiral domain formation nor any polarization current peaks and optical response on the applied fields can be found up to an electric field of  $33$  V<sub>pp</sub>μm<sup>-1</sup>. Therefore, introducing F substitution in this position favours tilt, reduces mesophase stability and removes polar order, which is mainly attributed to the unfavourable steric effect of fluorine in this inside-directed position. This is in line with previous observations made with rod-like molecules.<sup>[34]</sup>

<Table 4>

Using two lateral fluorine substituents at ortho and meta positions (series **23Fn**, Table 4) leads to higher transition temperatures compared to series **2Fn**, but lower if compared with the series **3Fn**. A nematic phase cannot be observed, and the SmA phase appears only as a monotropic phase for  $n = 10$ . Compounds with  $n \geq 12$  form exclusively the non-polar SmC<sub>s</sub><sup>[\*]</sup> phase, showing chiral conglomerates in homeotropic alignment (see Figure S18). Though chiral conglomerate formation indicates a paraelectric phase with SmC<sub>s</sub>P<sub>S</sub> domain structure no

polarization current peaks can be observed in triangular wave experiments (up to  $33 \text{ V}_{pp}\mu\text{m}^{-1}$ ). Due to the relatively high melting points and increased crystallization tendency, the temperature ranges with polar switching cannot be accessed for compounds **23Fn**.

A comparison of the effect of the azobenzene wings with respect to other rod-like units is given in the Supporting Discussion S5.1 in the SI.

### 3. Conclusions

Three series of bent-core molecules consisting of a 4-cyanoresorcinol-based central core and laterally fluorinated azobenzene wings have been synthesized and investigated, which provided fundamental insights into the development of polar order and spontaneous symmetry breaking by self-assembly of achiral bent-core molecules in lamellar LC phases (see Figure 1). It shows that already in the SmA phase locally tilted and polar  $\text{SmC}_s\text{P}_s$  domains emerge. With growing size of these ferroelectric domains macroscopic polar order develops continuously from the low permittivity SmA phases (SmA) via a series of uniaxial ( $\text{SmAP}_R$ ,  $\text{SmAP}_{AR}$ ) and biaxial ( $\text{SmC}_s\text{P}_R^{[*]}$ ,  $\text{SmC}_s\text{P}_{AR}$ ) high permittivity paraelectric smectic phases to the antiferroelectric polar smectic phases ( $\text{SmC}_s\text{P}_A$  and  $\text{SmC}_a\text{P}_A$ ). As known for the inorganic solid state ferroelectrics (e.g. perovskites)<sup>[15]</sup> the paraelectric-ferroelectric transition takes place by gradual changes of the polar domain size and by crossing a permittivity maximum temperature corresponding to the  $\text{SmAP}_{AR}$  -  $\text{SmCP}_A$  and  $/\text{SmC}_s\text{P}_{AR}$  -  $\text{SmCP}_A$  transitions (see Figure 9b),<sup>[37]</sup> which are the only transition of this process being associated with a small transition enthalpy (see Table 1). However, increasing polar coherence length leads to strengthening of antipolar correlation between the ferroelectric domains, thus giving rise to antiferroelectric switching already in the high permittivity paraelectric  $\text{SmAP}_{AR}$  and  $\text{SmC}_s\text{P}_{AR}$  ranges. Because the development of polar order is associated with the development of a tilted organization in the polar domains and a growing coherence of tilt between these domains, the paraelectric phases show unusual effects, as spontaneous symmetry breaking, non-classical electroclinic effects and field induced phase transitions. In the paraelectric phases and most  $\text{SmC}_s\text{P}_A$  phases the switching takes place by rotation around the molecular long axis, whereas only in the high polarization ( $B_2$ -like)  $\text{SmC}_a\text{P}_A$  phase with enhanced packing density it occurs by rotation on the tilt cone.

Core fluorination in the periphery appears to give increased electrostatic interactions between the aromatic cores, thus removing nematic phases and leading to enhanced smectic

phase stability, increased polar order and increased stability of chiral conglomerate type  $\text{SmC}^{[*]}$  phases. It also modifies the core packing, thus leading to reduced tilt and emergence of additional tilt randomized paraelectric  $\text{SmC}$  phases ( $\text{SmAP}_R$  and  $\text{SmAP}_{AR}$ ). These polar effects are dominating for core substitution in the peripheral 3-position, where steric effects are small. The importance of polar interactions is also evident from the effects of replacing F by Br and  $\text{CH}_3$ . In this order of decreasing electron acceptor ability the polar phases are destabilized and finally removed completely. Fluorination in the inside-directed 2-position strongly reduces smectic phase stability<sup>[34a]</sup> and polar order and removes superstructural chirality, due to the dominating steric distortion of the packing of the bent cores by F-substitution in this position.

Overall, this work provides clues for the understanding of the development of polar order in the LC phases of achiral bent-core mesogens depending on temperature, chain length and core-structure, and it indicates similarities to related transitions in solid state ferroelectrics. The advantage of fluid materials with polar response is their capability of being easily processible and addressable by a variety of external stimuli. The azo linkage in all reported compounds can undergo light-induced *trans*–*cis* isomerisation (see Supporting Discussion S5.2 in the SI for preliminary investigations in solution) which could in future work be used for optical addressing polar order and chirality.

#### 4. Experimental

**Synthesis.** - The benzoic acid **3an-3en** (2.4 mmol), synthesized according to the procedures given in the references,<sup>[38,64]</sup> were heated under reflux with excess  $\text{SOCl}_2$  (3 mL) and a catalytic amount DMF for one hour to give the corresponding benzoyl chloride **4an-4en**. The excess of thionyl chloride was removed under reduced pressure. The formed benzoyl chloride was then dissolved in dry  $\text{CH}_2\text{Cl}_2$  (20 mL) and 1.2 mmol of 4-cyanoresorcinol **5**<sup>[28]</sup> previously dissolved in  $\text{CH}_2\text{Cl}_2$  (10 mL) was added to that solution, followed by addition of triethylamine (2.8 mmol) and a catalytic amount of pyridine. The reaction mixture was then refluxed for 6 hrs under an argon atmosphere. The reaction mixture was cooled to room temperature and washed with 10% HCl (2 × 50 mL) and with cold water (2 × 50 mL). The aqueous phase was extracted with  $\text{CH}_2\text{Cl}_2$  (3 × 50 mL) and the combined organic phases were dried over anhydrous  $\text{Na}_2\text{SO}_4$ . The crude residue obtained after removal of solvent was purified by chromatography on silica gel using chloroform as eluent affording an orange material which was crystallized from chloroform/ethanol mixture to

give the final bent core compounds. The analytical data of **3F12**, **2F12** and **23F12** are given as representative examples below; the analytical data for all other reported compounds are collated in the Supporting Information (SI).

**4-Cyano-1,3-phenylene bis-[4-(3-fluoro-4-dodecyloxyphenylazo)benzoate] (3F12).** Orange powder, yield 68 %,  $^1\text{H-NMR}$  (400 MHz,  $\text{CDCl}_3$ ):  $\delta$  8.40 (d,  $J = 8.5$  Hz, 2H, Ar-H), 8.33 (d,  $J = 8.5$  Hz, 2H, Ar-H), 8.07–7.93 (m, 4H, Ar-H), 7.83 (d,  $J = 8.6$  Hz, 3H, Ar-H), 7.79–7.70 (m, 2H, Ar-H), 7.59 (d,  $J = 2.2$  Hz, 1H, Ar-H), 7.36 (dd,  $J = 8.5, 2.2$  Hz, 1H, Ar-H), 7.10 (t,  $J = 8.6$  Hz, 2H, Ar-H), 4.14 (t,  $J = 6.6$  Hz, 4H,  $\text{OCH}_2\text{CH}_2$ ), 1.95–1.81 (m, 4H,  $\text{OCH}_2\text{CH}_2$ ), 1.60–1.16 (m, 36H,  $\text{CH}_2$ ), 0.88 (t,  $J = 6.7$  Hz, 6H,  $\text{CH}_3$ ).  $^{13}\text{C-NMR}$  (126 MHz,  $\text{CDCl}_3$ ):  $\delta$  163.44 (COOAr), 163.08 (–COOAr), 155.89 ( $\text{C}_{\text{Ar-O-CH}_2}$ ), 155.79 ( $\text{C}_{\text{Ar-O-CH}_2}$ ), 154.77, 153.87, 153.45, 151.89, 150.92, 150.87, 150.83, 150.78, 146.46, 146.43, 146.39, 133.99, 131.65, 131.41, 129.57, 129.19, 123.94, 123.93, 122.89, 122.82, 120.01, 117.34, 114.73 (CN), 113.44, 113.41, 107.96, 107.89, 107.81, 107.74, 104.28 ( $\text{C}_{\text{Ar-CN}}$ ), 69.56 ( $\text{C}_{\text{Ar-O-CH}_2}$ ), 31.89, 29.63, 29.61, 29.56, 29.51, 29.32, 29.31, 29.04, 25.87, 22.67, 14.09 ( $\text{CH}_3$ ).  $^{19}\text{F-NMR}$  (470 MHz,  $\text{CDCl}_3$ )  $\delta$  -132.27 – -132.73 (m). Elemental Analysis: Calc. for  $\text{C}_{57}\text{H}_{67}\text{F}_2\text{N}_5\text{O}_6$  C, 71.60; H, 7.06; N, 7.32. Found C, 71.63; H, 7.00; N, 7.31 %.

**4-Cyano-1,3-phenylene bis-[4-(2-fluoro-4-dodecyloxyphenylazo)benzoate] (2F12).** Orange powder, yield 66 %,  $^1\text{H-NMR}$  (400 MHz,  $\text{CDCl}_3$ )  $\delta$  8.39 (d,  $J = 8.5$  Hz, 2H, Ar-H), 8.32 (d,  $J = 8.5$  Hz, 2H, Ar-H), 8.07 – 7.97 (m, 4H, Ar-H), 7.89 – 7.78 (m, 3H, Ar-H), 7.59 (d,  $J = 2.2$  Hz, 1H, Ar-H), 7.36 (dd,  $J = 8.5, 2.2$  Hz, 1H, Ar-H), 6.82 – 6.73 (m, 4H, Ar-H), 4.04 (t,  $J = 6.5$  Hz, 4H,  $\text{OCH}_2\text{CH}_2$ ), 1.89 – 1.76 (m, 4H,  $\text{OCH}_2\text{CH}_2$ ), 1.64 – 1.17 (m, 36H,  $\text{CH}_2$ ), 0.88 (t,  $J = 6.8$  Hz, 6H,  $\text{CH}_3$ ).  $^{13}\text{C-NMR}$  (126 MHz,  $\text{CDCl}_3$ ):  $\delta$  164.09 (COOAr), 164.05 (COOAr), 164.01 ( $\text{C}_{\text{Ar-O-CH}_2}$ ), 163.96 ( $\text{C}_{\text{Ar-O-CH}_2}$ ), 163.46, 163.20, 163.11, 161.13, 156.33, 156.22, 154.78, 153.46, 134.93, 134.89, 134.87, 134.84, 133.97, 131.63, 131.39, 129.47, 129.09, 122.96, 122.89, 120.00, 118.59, 118.56, 117.36, 114.74 (CN), 111.56, 111.54, 111.52, 111.49, 104.28 ( $\text{C}_{\text{Ar-CN}}$ ), 102.42, 102.23, 68.93 ( $\text{C}_{\text{Ar-O-CH}_2}$ ), 68.92 ( $\text{C}_{\text{Ar-O-CH}_2}$ ), 31.87, 29.63, 29.61, 29.55, 29.52, 29.32, 29.30, 28.97, 25.92, 22.66, 14.09 ( $\text{CH}_3$ ).  $^{19}\text{F-NMR}$  (470 MHz,  $\text{CDCl}_3$ ):  $\delta$  -119.77 – -120.14 (m). Elemental Analysis: Calc. for  $\text{C}_{57}\text{H}_{67}\text{F}_2\text{N}_5\text{O}_6$  C, 71.60; H, 7.06; N, 7.32. Found C, 71.60; H, 7.11; N, 7.38 %.

**4-Cyano-1,3-phenylene bis-[4-(2,3-difluoro-4-dodecyloxyphenylazo)benzoate] (23F12).** Orange powder, yield 68 %,  $^1\text{H-NMR}$  (400 MHz,  $\text{CDCl}_3$ )  $\delta$  8.40 (d,  $J = 8.5$  Hz, 2H, Ar-H), 8.32 (d,  $J = 8.5$  Hz, 2H, Ar-H), 8.09 – 7.97 (m, 4H, Ar-H), 7.83 (d,  $J = 8.6$  Hz, 1H, Ar-H), 7.67 – 7.54 (m, 3H, Ar-H), 7.36 (dd,  $J = 8.5, 2.1$  Hz, 1H, Ar-H), 6.88 – 6.76 (m, 2H, Ar-H), 4.15 (t,  $J = 6.6$  Hz, 4H,  $\text{OCH}_2\text{CH}_2$ ), 1.95 – 1.80 (m, 4H,  $\text{OCH}_2\text{CH}_2$ ), 1.68 – 1.14 (m, 36H,  $\text{CH}_2$ ), 0.88 (t,  $J = 6.6$  Hz, 6H,  $\text{CH}_3$ ).  $^{13}\text{C-NMR}$  (126 MHz,  $\text{CDCl}_3$ ):  $\delta$  163.37 (COOAr), 163.01 (COOAr), 156.02 ( $\text{C}_{\text{Ar-O-CH}_2}$ ), 155.92 ( $\text{C}_{\text{Ar-O-CH}_2}$ ), 154.73, 153.42, 151.95, 151.19, 151.10, 149.11, 149.02, 142.68, 142.58, 140.70, 140.60, 135.55, 135.52, 135.49, 134.00, 131.66, 131.42, 129.93, 129.55, 123.13, 123.06, 120.03, 117.33, 114.70 (CN), 111.98, 111.95, 108.46, 104.31 ( $\text{C}_{\text{Ar-CN}}$ ), 70.08 ( $\text{C}_{\text{Ar-O-CH}_2}$ ), 31.89, 29.62, 29.60, 29.54, 29.49, 29.32, 29.27, 29.02, 25.80, 22.66, 14.08 ( $-\text{CH}_3$ ).  $^{19}\text{F-NMR}$  (470 MHz,  $\text{CDCl}_3$ ):  $\delta$  -145.72 – -146.13 (m), -157.86 – -158.19 (m). Elemental Analysis: Calc. for  $\text{C}_{57}\text{H}_{65}\text{F}_4\text{N}_5\text{O}_6$  C, 69.00; H, 6.60; N, 7.06. Found C, 68.98; H, 6.61; N, 6.99 %.

**Analytical methods.** - Thin layer chromatography (TLC) was performed on aluminium sheet precoated with silica gel. Starting materials were obtained from commercial sources and used without further purification. The solvents were dried using the standard methods when required. The purity and the chemical structures of all synthesized compounds were confirmed by the spectral data. The structure characterization of the synthesized bent-core compounds is based on  $^1\text{H-NMR}$ ,  $^{13}\text{C-NMR}$  and  $^{19}\text{F-NMR}$  (Varian Unity 400 spectrometer, in  $\text{CDCl}_3$  solutions, with tetramethylsilane as internal standard). Microanalyses were performed using a Leco CHNS-932 elemental analyzer.

**Investigation methods.** - The phase behaviour of the synthesized compounds has been investigated by polarizing optical microscopy (PLM), differential scanning calorimetry (DSC), X-ray diffraction (XRD) studies and electro-optical measurements. All compounds are thermally stable as confirmed by the reproducibility of thermograms on several heating and cooling cycles. The assignment of the mesophases was made on the basis of combined results of optical textures, electro optical studies and XRD. For optical microscopy an Optiphot 2, polarizing microscope (Nikon) in conjunction with a heating stage (FP82HT, Mettler) was used. Photoisomerization of the azobenzene group is negligible under the used experimental conditions so that formation of *trans-cis* mixtures can be excluded. Differential scanning calorimetry (DSC) was performed using a DSC-7 (Perkin Elmer) with a scanning rate of  $10 \text{ K min}^{-1}$ . X-ray diffraction (XRD) was

done at Cu-K $\alpha$  line ( $\lambda = 1.54 \text{ \AA}$ ) using standard Coolidge tube source with a Ni-filter. Investigations of oriented samples were performed using a 2D-detector (H1-Star, Siemens AG). Uniform orientation was achieved by alignment in a magnetic field ( $B \approx 1\text{T}$ ) using thin capillaries. The orientation once achieved is maintained by slow cooling ( $0.1 \text{ K min}^{-1}$ ) in the presence of the magnetic field. Electro-optical experiments have been carried out using a home built electro-optical setup under an applied triangular wave voltage in commercially available indium tin oxide (ITO) coated glass cells (E.H.C., Japan, polyimide (PI) coated for planar alignment, antiparallel rubbing, thickness 6 and 10  $\mu\text{m}$  and measuring area  $1 \text{ cm}^2$ ).

**Supporting Information.** Synthesis and analytical data of the compounds, additional experimental data (DSC traces, textures, XRD data, polarization current curves and electrooptical studies) and supporting discussion (effects of core structure and photoisomerization in solution)

**Acknowledgements.** The work was supported by the DFG (Grant Ts 39/24-1).

## References

- [1] A. Zielinska, M. Leonowicz, H. Li, T. Nakanishi, *Curr Opin Coll. Interf. Sci.* **2014**, *19*, 131–139.
- [2] C. Tschierske, *Angew. Chem.* **2013**, *125*, 8992-9047; *Angew. Chem. Int. Ed.* **2013**, *52*, 8828-8878.
- [3] J. W. Goodby, P. J. Collings, T. Kato, C. Tschierske, H. F. Gleeson, P. Raynes, eds., *Handbook of Liquid Crystals*, 2nd Ed., Wiley-VCH, Weinheim **2014**.
- [4] a) S. Yang, Y. Liu, H. Tan, C. Wu, Z. Wu, G. Shena, R. Yua, *Chem. Commun.* **2012**, *48*, 2861-2863; b) T. Kato, N. Mizoshita, K. Kishimoto, *Angew. Chem.* **2006**, *118*, 44-74; *Angew. Chem. Int. Ed.* **2006**, *45*, 38-68; c) S. Kumar, *Chem. Soc. Rev.* **2006**, *35*, 83-109; d) E.-K. Fleischmann, R. Zentel, *Angew. Chem.* **2013**, *125*, 8972–8991; *Angew. Chem. Int. Ed.* **2013**, *52*, 8810-8827.
- [5] a) I. Tahar-Djebbar, F. Nekelson, B. Heinrich, B. Donnio, D. Guillon, D. Kreher, F. Mathevet, A. J. Attias, *Chem. Mater.* **2011**, *23*, 4653-4656; b) T. Donaldson, P. A. Henderson, M. F. Achard, C. T. Imrie, *J. Mater. Chem.* **2011**, *21*, 10935-10941; c) O. Yaroshchuk, Y. Reznikov, *J. Mater. Chem.* **2012**, *22*, 286-300.
- [6] a) G. C. Kuang, X. R. Jia, M. J. Teng, E. Q. Chen, W. S. Li, Y. Ji, *Chem. Mater.* **2012**, *24*, 71-80; b) J. Vergara, N. Gimeno, M. Cano, J. Barber, P. Romero, J. L. Serrano, M. B. Ros, *Chem. Mater.* **2011**, *23*, 4931-4940.
- [7] J. F. Stoddart, *Nature Chem.* **2009**, *1*, 5-15.
- [8] a) A. S. Tayi, A. K. Shveyd, A. C.-H. Sue, J. M. Szarko, B. S. Rolczynski, D. Cao, T. J. Kennedy, A. A. Sarjeant, C. L. Stern, W. F. Paxton, W. Wu, S. K. Dey, A. C. Fahrenbach, J. R. Guest, H. Mohseni, L. X. Chen, K. L. Wang, J. F. Stoddart, S. I. Stupp, *Nature*. **2012**, *488*, 485-489; b) A. S. Tayi, A. Kaeser, M. Matsumoto, T. Aida, S. I. Stupp, *Nature Chem.* **2015**, *7*, 281-294.
- [9] a) S. T. Lagerwall, *Ferroelectric and Antiferroelectric Liquid Crystals*, Wiley-VCH, Weinheim, **1999**; b) H.-S. Kitzerow, C. Bahr, *Chirality in Liquid Crystals*, Springer, New York, **2001**.
- [10] D. Miyajima, F. Araoka, H. Takezoe, J. Kim, K. Kato, M. Takata, T. Aida, *Science*. **2012**, *336*, 209-213.

- [11] T. Niori, J. Sekine, J. Watanabe, T. Furukava, H. Takezoe, *J. Mater. Chem.* **1996**, *6*, 1231-1233.
- [12] D. Shen, A. Pegenau, S. Diele, I. Wirth, C. Tschierske, *J. Am. Chem. Soc.* **2000**, *122*, 1593-1601.
- [13] a) G. Pelzl, S. Diele, W. Weissflog, *Adv. Mater.* **1999**, *11*, 707-724; b) R. A. Reddy, C. Tschierske, *J. Mater. Chem.* **2006**, *16*, 907-961; c) H. Takezoe, Y. Takanishi, *Jpn. J. Appl. Phys.* **2006**, *45*, 597; d) A. Eremin, A. Jákli, *Soft Matter*. **2013**, *9*, 615-637.
- [14] D. R. Link, G. Natale, R. Shao, J. E. MacLennan, N. A. Clark, E. Körblova, D. M. Walba, *Science*. **1997**, *278*, 1924-1927.
- [15] a) T. M. Shaw, S. Trolier-McKinstry, P. C. McIntyre, *Annu. Rev. Mater. Sci.* **2000**, *30*, 263-298; b) R. Waser, O. Lohse, *Integrated Ferroelectrics*. **1998**, *21*, 27; c) J.-H. Park, Y. Kim, *J. Korean Phys. Soc.* **1998**, *32*, 967-969.
- [16] a) G. Pelzl, W. Weissflog, In *Thermotropic Liquid Crystals: Recent Advances* (Ed. A. Ramamoorthy), Springer, The Netherlands, **2007**, pp. 1-58; b) W. Weissflog, H. N. S. Murthy, S. Diele, G. Pelzl, *Phil. Trans. Royal Soc. A*. **2006**, *364*, 2657-2679.
- [17] J. P. F. Lagerwall, F. Giesselmann, M. D. Wand, D. M. Walba, *Chem. Mater.* **2004**, *16*, 3606-3615.
- [18] Y. P. Panarin, M. Nagaraj, S. Sreenilayam, J. K. Vij, A. Lehmann, C. Tschierske, *Phys. Rev. Lett.* **2011**, *107*, 247801.
- [19] M. Alaasar, M. Prehm, M. Poppe, M. Nagaraj, J. K. Vij, C. Tschierske, *Soft Matter*. **2014**, *10*, 5003-5016.
- [20] S. P. Sreenilayam, Y. P. Panarin, J. K. Vij, V. P. Panov, A. Lehmann, M. Poppe, M. Prehm, C. Tschierske, *Nature Commun.* **2016**, *7*, 11369, DOI: 10.1038/ncomms11369.
- [21] F. C. Yu, L. J. Yu, *Chem. Mater.* **2006**, *18*, 5410-5420.
- [22] A. Eremin, S. Stern, R. Stannarius, *Phys. Rev. Lett.* **2008**, *101*, 247802.
- [23] a) P. Sathyanarayana, S. Radhika, B. K. Sadashiva, S. Dhara, *Soft Matter*. **2012**, *8*, 2322-2327; b) D. Malkar, B. K. Sadashiva, A. Roy, *Soft Matter*. **2016**, *12*, 4960-4966.
- [24] M. Horčič, V. Kozmík, J. Svoboda, V. Novotná, D. Pocięcha, *J. Mater. Chem. C*. **2013**, *1*, 7560-7567.
- [25] R. K. Nath, R. Deb, N. Chakraborty, G. Mohiuddin, D. S. S. Raob,; N.V. S. Rao, *J. Mater. Chem. C*. **2013**, *1*, 663-670.

- [26] W. Weissflog, U. Baumeister, M. G. Tamba, G. Pelzl, H. Kresse, R. Friedemann, G. Hempel, R. Kurz, M. Roos, K. Merzweiler, A. Jákli, C. Zhang, N. Diorio, R. Stannarius, A. Eremine, U. Korneke, *Soft Matter*. **2012**, *8*, 2671-2685.
- [27] a) I. Wirth, S. Diele, A. Eremin, G. Pelzl, S. Grande, L. Kovalenko, N. Pancenko, W. Weissflog, *J. Mater. Chem.* **2001**, *11*, 1642-1650; b) L. Kovalenko, M. W. Schröder, R. A. Reddy, S. Diele, G. Pelzl, W. Weissflog, *Liq. Cryst.* **2005**, *32*, 857-865.
- [28] C. Keith, A. Lehmann, U. Baumeister, M. Prehm, C. Tschierske, *Soft Matter*. **2010**, *6*, 1704-1721.
- [29] A. Eremin, M. Floegel, U. Kornek, S. Stern, R. Stanarius, H. Nadasi, W. Weissflog, C. Zhu, Y. Shen, C. S. Park, J. Maclennan, N. Clark, *Phys. Rev. E*. **2012**, *86*, 051701.
- [30] H. M. D. Bandara, S. C. Burdette, *Chem. Soc. Rev.* **2012**, *41*, 1809-1825.
- [31] M. Alaasar, *Liq. Cryst.* **2016**, *43*, 2208-2243.
- [32] a) M. Alaasar, M. Prehm, M. Nagaraj, J. K. Vij, C. Tschierske, *Adv. Mater.* **2013**, *25*, 2186-2191; b) M. Alaasar, M. Prehm, K. May, A. Eremin, C. Tschierske, *Adv. Funct. Mater.* **2014**, *24*, 1703-1717; c) M. Alaasar, M. Prehm, C. Tschierske, *Chem. Eur. J.* **2016**, *22*, 6583-6597; d) M. Alaasar, M. Prehm, C. Tschierske, *Chem. Commun.* **2013**, *49*, 11062-11064.
- [33] C. Tschierske, *Top. Curr. Chem.* **2012**, *318*, 1-108.
- [34] a) M. Hird, *Chem. Soc. Rev.* **2007**, *36*, 2070-2095; b) F. Guittard, E. Taffin de Givenchy, S. Geribaldi and A. Cambon, *J. Fluorine Chem.* **1999**, *100*, 85-96; c) J. W. Goodby, I. M. Saez, S. J. Cowling, J. S. Gasowska, R. A. MacDonald, S. Sia, P. Watson, K. J. Toyne, M. Hird, R. A. Lewis, S. E. Lee, V. Vaschenko, *Liq. Cryst.* **2009**, *36*, 567-605.
- [35] M. Bremer, P. Kirsch, M. Klasen-Memmer, K. Tarumi, *Angew. Chem.* **2013**, *125*, 9048-9065; *Angew. Chem. Int. Ed.* **2013**, *52*, 8880-8896.
- [36] a) J. P. Bedel, J. C. Rouillon, J. P. Marcerou, M. Laguerre, H. T. Nguyen, M. F. Achard, *J. Mater. Chem.* **2002**, *12*, 2214-2220; b) R. A. Reddy, B. K. Sadashiva, *J. Mater. Chem.* **2002**, *12*, 2627-2632; c) H. N. Shreenivasa Murthy, B. K. Sadashiva, *Liqu. Cryst.* **2004**, *31*, 1337-1346; d) G. Dantlgraber, D. Shen, S. Diele, C. Tschierske, *Chem. Mater.* **2002**, *14*, 1149-1158; e) C. V. Yelamaggad, I. Swamy Shashikala, U. S. Hiremath, G. Liao, A. Jakli, D. S. Shankar Rao, S. Krishna Prasad, Q. Li, *Soft Matter* **2006**, *2*, 785-792; f) K. M. Fergusson, M. Hird, *J. Mater. Chem.* **2010**, *20*, 3069-3078;

- [37] M. Alaasar, M. Prehm, M.-G. Tamba, N. Sebastian, A. Eremin, C. Tschierske, *ChemPhysChem*. **2016**, *17*, 278-287.
- [38] Alaasar, M.; Prehm, M.; Cao, Y.; Liu, F.; Tschierske, C. *Angew. Chem.* **2016**, *128*, 320 – 324; *Angew. Chem. Int. Ed.* **2016**, *55*, 312-316.
- [39] N. Vaupotic, J. Szydłowska, M. Salamonczyk, A. Kovarova, J. Svoboda, M. Osipov, D. Pociecha, E. Gorecka, *Phys. Rev. E*. **2009**, *80*, 030701(R).
- [40] C. Tschierske, D. J. Photinos, *J. Mater. Chem.* **2010**, *20*, 4263-4294.
- [41] a) A. De Vries, *J. Chem. Phys.* **1979**, *71*, 25-31; b) S. T. Lagerwall, P. Rudquist, F. Giesselmann, *Mol. Cryst. Liq. Cryst.* **2009**, *510*, 148-157; c) for a review see J. P. F. Lagerwall, F. Giesselmann, *ChemPhysChem*. **2006**, *7*, 20-45.
- [42] a) D. Pociecha, M. Cepic, E. Gorecka, J. Mieczkowski, *Phys. Rev. Lett.* **2003**, *91*, 185501; b) Y. Shimbo, E. Gorecka, D. Pociecha, F. Araoka, M. Goto, Y. Takanishi, K. Ishikawa, J. Mieczkowski, K. Gomola, H. Takezoe, *Phys. Rev. Lett.* **2006**, *97*, 113901; c) K. Gomola, L. Guo, S. Dhara, Y. Shimbo, E. Gorecka, D. Pociecha, J. Mieczkowski, H. Takezoe, *J. Mater. Chem.* **2009**, *19*, 4240-4247; d) L. Guo, K. Gomola, E. Gorecka, D. Pociecha, S. Dhara, F. Araoka, K. Ishikawa, H. Takezoe, *Soft Matter*. **2011**, *7*, 2895-2899.
- [43] C. Keith, M. Prehm, Y. P. Panarin, J. K. Vij, C. Tschierske, *Chem. Commun.* **2010**, *46*, 3702-3704.
- [44] M. Gupta, S. Datta, S. Radhika, B. K. Sadashiva, A. Roy, *Soft Matter*. **2011**, *7*, 4735-4741.
- [45] H. Ocak, M. Poppe, B. Bilgin-Eran, G. Karanlık, M. Prehm, C. Tschierske, *Soft Matter*. **2016**, *12*, 7405-7422.
- [46] H. N. S. Murthy, M. Bodyagin, S. Diele, U. Baumeister, G. Pelzl, W. Weissflog, *J. Mater. Chem.* **2006**, *16*, 1634-1643.
- [47] K. Gomola, L. Guo, D. Pociecha, F. Araoka, K. Ishikawa, H. Takezoe, *J. Mater. Chem.* **2010**, *20*, 7944-7952.
- [48] Previously a SmAP<sub>A</sub> domain structure was proposed for this phase and the temperature dependent phase sequence SmAP<sub>R</sub>-SmAP<sub>AR</sub> was inverted.<sup>[47]</sup>
- [49] N. Sebastian, S. Belau, A. Eremin, M. Alaasar, M. Prehm C. Tschierske, *Phys. Chem. Chem. Phys.*, **2017**, DOI: 10.1039/c6cp08145b.
- [50] In ref. 32b the SmC<sub>s</sub>P<sub>AR</sub> phase of related non-fluorinated compounds was designated as SmC<sub>s</sub>P<sub>S</sub>, based on preliminary investigations in FS films, indicating the presence of large

---

SmC<sub>S</sub>P<sub>S</sub> domains. In ref. 37 the same phase was reported for **3F20** and this phase was renamed SmC<sub>S</sub>P<sub>AR</sub> based on the dielectric investigations and considering the presence of two polarization current peaks in each half cycle of the applied triangular voltage.

- [51] a) A. Eremin, H. Nadasi, G. Pelzl, S. Diele, H. Kresse, W. Weissflog, S. Grande, *Phys. Chem. Chem. Phys.* **2004**, *6*, 1290-1298; b) D. Pocięcha, E. Gorecka, M. Cepic, N. Vaupotic, K. Gomola, J. Mieczkowski, *Phys. Rev. E* **2005**, *72*, 060701(R); c) D. Pocięcha, E. Gorecka, M. Cepic, N. Vaupotic, W. Weissflog, *Phys. Rev. E* **2006**, *74*, 021702.
- [52] a) C. Dressel, T. Reppe, M. Prehm, M. Brautzsch, C. Tschierske, *Nature Chem.* **2014**, *6*, 971-977; b) C. Tschierske, G. Ungar, *ChemPhysChem* **2016**, *17*, 9-26.
- [53] M. Alaasar, M. Prehm, M. Brautzsch, C. Tschierske, *Soft Matter* **2014**, *10*, 7285-7296.
- [54] An inversion of the dark extinctions is observed because some polar order is retained at 0V, most probably in the surface layers which then acts as command layers determining the tilt direction in the bulk sample (see Figure 7n-q).
- [55] a) J. Szydłowska, J. Mieczkowski, J. Matraszek, D. W. Bruce, E. Gorecka, D. Pocięcha, D. Guillon, *Phys. Rev. E: Stat., Nonlinear, Soft Matter Phys.* **2003**, *67*, 031702; b) C. Keith, R. A. Reddy, U. Baumeister, C. Tschierske, *J. Am. Chem. Soc.* **2004**, *126*, 14312-14313; c) M. Nakata, R. F. Shao, J. E. Maclennan, W. Weissflog, N. A. Clark, *Phys. Rev. Lett.* **2006**, *96*, 067802.
- [56] a) C. Keith, R. A. Reddy, A. Hauser, U. Baumeister, C. Tschierske, *J. Am. Chem. Soc.* **2006**, *128*, 3051-3066; b) C. Keith, R. A. Reddy, M. Prehm, U. Baumeister, H. Kresse, J. L. Chao, H. Hahn, H. Lang, C. Tschierske, *Chem. Eur. J.* **2007**, *13*, 2556-2577.
- [57] Y. Zhang, U. Baumeister, C. Tschierske, M. O'Callaghan, C. Walker, *Chem. Mater.* **2010**, *22*, 2869-2884.
- [58] G. Dantlgraber, A. Eremin, S. Diele, A. Hauser, H. Kresse, G. Pelzl, C. Tschierske, *Angew. Chem.* **2002**, *114*, 2514-2518; *Angew. Chem. Int. Ed.* **2002**, *41*, 2408-2412.
- [59] E. Westphal, H. Gallerdo, G. F. Caramori, N. Sebastian, M.-G. Tamba, A. Eremin, S. Kawauchi, M. Prehm, C. Tschierske, *Chem. Eur. J.* **2016**, *22*, 8181-8197.
- [60] R. A. Reddy, C. Zhu, R. Shao, E. Korblova, T. Gong, Y. Shen, E. Garcia, M. A. Glaser, J. E. Maclennan, D. M. Walba, N. A. Clark, *Science*, **2011**, *332*, 72-77.
- [61] a) C. Tschierske, *J. Mater. Chem.* **1998**, *8*, 1485-1508; b) C. Tschierske, *Isr. J. Chem.* **2012**, *52*, 935-959.

- 
- [62] a) Hunter, C. A.; Sanders, J. K. M. *J. Am. Chem. Soc.* **1990**, *112*, 5525–5534; b) Martinez, C. R.; Iverson, B. L. *Chem. Sci.* **2012**, *3*, 2191–2201.
- [63] Immirzi, A.; Perini, B. *Acta Crystallogr. Sect. A.* **1977**, *33*, 216-218.
- [64 ] a) M. Alaasar M. Prehm M. Brautzsch C. Tschierske. *J. Mater. Chem. C.* **2014**, *2*, 5487.

**Scheme 1.** Development of a) polar order ( $P_S$  = synpolar,  $P_A$  = antipolar) and b) tilt ( $C_s$  = synclinic,  $C_a$  = anticlinic) and chirality (red/blue color) in the lamellar phases of bent-core LCs; c) chemical structures of the considered 4-cyanoresorcinol bases BCLCs.

**Scheme 2.** Synthesis of the bent-core mesogens (intermediates: **a**: X = F, Y = H; **b**: X = H, Y = F; **c**: X = Y = F; **d**: X = Br, Y = H and **e**: X = CH<sub>3</sub>, Y = H; for the structures of the bent-core mesogens see also Scheme 1c).

**Figure 1.** a) Plot of the transition temperatures of compounds **3Fn** as a function of the alkyl chain length ( $n$ ). The solid black line indicates the crystallization temperature on cooling; the colored lines indicate the upper temperature limits for the corresponding mesophases; colored areas visualize the molecular organization (yellow = nematic, red = SmA ranges and green SmC ranges); the square grid pattern indicates LC phases composed of ferroelectric domains and the parallel line pattern (bottom) LC phases composed of polar layers; b) shows simplified models of the fundamental phase structures under discussion and their development depending on temperature and alkyl chain length; dots and crosses indicate opposite polar directions, red/blue indicate opposite chirality; the abbreviations are explained in Table 1; for the tilt randomized SmAP<sub>AR</sub> structure only one chirality is shown, though on a larger scale the structure is racemic (see also Figure 6b).

**Figure 2.** XRD patterns of a magnetically aligned sample of compound **3F6**: a, b) in the N<sub>CyBA</sub> phase at 122 °C and c, d) in the SmA phase at 110 °C; a, c) represent the complete patterns after subtraction of the scattering in the isotropic liquid state at 130 °C and b, d) show the small angle patterns, the insets in a, c) show the corresponding optical textures (between crossed polarizers, horizontal and vertical) in planar alignment (see also Figure S7).

**Figure 3.** Temperature dependence of the  $d$ -value of compounds a) **3F8**, ( $L_{mol} = 5.1$  nm), b) **3F10** ( $L_{mol} = 5.6$  nm), c) **3F12** ( $L_{mol} = 6.1$  nm) and d) **3F14** ( $L_{mol} = 6.6$  nm) measured by SAXS on cooling down to the crystallization temperature;  $L_{mol}$  was determined as shown in Figure S9; note that the tilt already arises in the SmA range, so that the SmA-SmC phase transitions do not correspond to the maxima of the  $d$ -values; data points in the Iso range refer to the maxima of the diffuse small angle scattering.

**Figure 4.** Switching current response curves and textures of compound **3F8** (6  $\mu\text{m}$  PI coated ITO cell). a-d). Polarization current response curves on applying a triangular wave field (20  $\text{V}_{\text{pp}}\mu\text{m}^{-1}$ , 10 Hz); e-g) textures as observed for planar samples (molecules parallel to the substrate surfaces) between crossed polarizers e) in the  $\text{SmAP}_{\text{AR}}$  phase, f) at the  $\text{SmAP}_{\text{AR}}\text{-SmC}_a\text{P}_A$  transition and g) in the  $\text{SmC}_a\text{P}_A$  phase; the insets show the corresponding textures in homeotropic alignment (layers parallel to the substrate surfaces) as observed between non-treated microscopy glass plates; the temperature dependence of the polarization is displayed in Figure 5a and DSCs are shown in Figure S6a.

**Figure 5.** a,b) Development of polarization depending on temperature (26.7  $\text{V}_{\text{pp}}\mu\text{m}^{-1}$ , 10 Hz) for a) **3F8**, b) **3F10** and c) **3F12** and d) **3F14** as observed on cooling solid lines indicate phase transitions associated with a transition enthalpy whereas dashed lines indicate continuous transitions.

**Figure 6.** Textures as observed in DC field experiments in the  $\text{SmAP}_{\text{AR}}$  phase range of **3F8** at  $T = 108\text{ }^\circ\text{C}$ : a) before application of an E-field, c) under the E-field and after reversal of the field and e) after removal of the applied field (planar ITO cell between crossed polarizers see arrows in a)); b, d, f) shows the models of the molecular organization in the distinct states; R is the rubbing direction.

**Figure 7.** a-e) Switching current response curves of compound **3F12** on applying a triangular wave field (10 Hz in 6  $\mu\text{m}$  ITO cell); f-h, j-l, n-p, r-t) textures as observed between crossed polarizers in DC field experiments at  $+6.7\text{ V}\mu\text{m}^{-1}$  (left column), 0 V (middle column) and  $-6.7\text{ V}\mu\text{m}^{-1}$  (right column) and i, m, q, u) models of the molecular reorganization in the switching processes. The green color in o, s) corresponds to the next lower order of birefringence, due to the intense yellow/orange color of the azo compound blue and purple birefringence colors appear green; for DSCs, see Figure S6c.

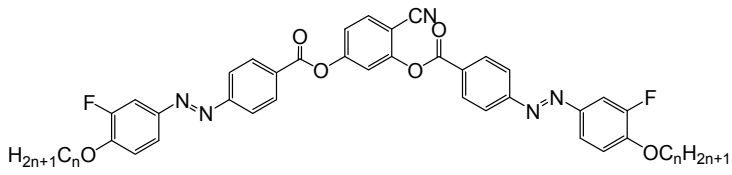
**Figure 8.** Optical textures of the homeotropic aligned (layers parallel to the substrate surfaces)  $\text{SmC}_s\text{P}_R^{[*]}$  phase of **3F12** at  $T = 133\text{ }^\circ\text{C}$ , b) between crossed polarizers and a,c) between slightly

decrossed polarizers, decrossed in opposite directions, thus indicating the optical activity of the distinct domains.

**Figure 9.** a) Spontaneous polarization ( $P_s$ ) in the  $\text{SmC}_a\text{P}_A$  phases depending on alkyl chain length ( $n$ ), measured at  $T = 95\text{ }^\circ\text{C}$  (for **3F20** at  $T = 90\text{ }^\circ\text{C}$ ) under an applied field of  $26.7\text{ V}_{\text{pp}}\ \mu\text{m}^{-1}$  at 10 Hz and b) temperature dependence of the static dielectric permittivity ( $\epsilon$ ) of compound **3F20** (reproduced from ref.<sup>[37]</sup> with adjustment to the phase designation used herein; dashed lines indicate continuous transitions).

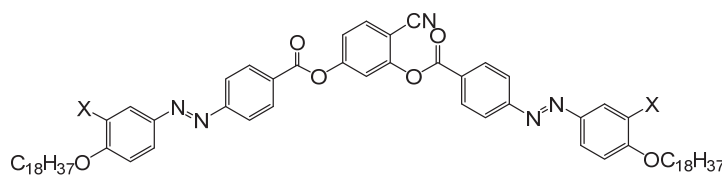
**Figure 10.** Effects of molecular rotations (top line) and out-of-layer fluctuations (green arrows, middle) on the mesophase structure of the tilted smectic phases formed by molecules with shapes at the transition from linear to bend.

**Figure 11.** Plot of the transition temperatures of compounds  $\mathbf{Hn}^{[32a,b]}$  as a function of the alkyl chain length ( $n$ ); the solid black line indicates the crystallization temperature on cooling, the coloured lines indicate the upper temperature limits for the distinct mesophases; modified with adjustment to the phase designation used herein; abbreviations:  $\text{N}_{\text{CycbC}}$  = cybotactic nematic phase composed of SmC clusters;  $\text{Col}_{\text{rec}}$  = rectangular columnar ribbon phase ( $\text{B}_1$  phase);  $\text{M}_1$  = unknown mesophase with high viscosity, for other abbreviations see Table 1 and Fig 1b.

**Table 1.** Phase transitions of compounds **3Fn**.<sup>a</sup>


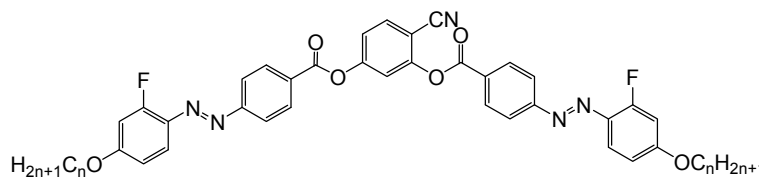
Comp.	<i>n</i>	<i>T</i> / °C [Δ <i>H</i> /kJ·mol <sup>-1</sup> ]
<b>3F4</b>	4	Cr 164 (N <sub>cybA</sub> 136) Iso [108.2] [0.9]
<b>3F6</b>	6	Cr 112 (SmAP <sub>AR</sub> 101) SmAP <sub>R</sub> 117 N <sub>cybA</sub> 128 Iso [49.3] [-] [0.2] [0.9]
<b>3F8</b>	8	Cr 112 (SmC <sub>a</sub> P <sub>A</sub> 104 SmAP <sub>AR</sub> 110) SmAP <sub>R</sub> 137 Iso [60.7] [3.4] [-] [3.2]
<b>3F10</b>	10	Cr 108 (SmC <sub>a</sub> P <sub>A</sub> 108) SmC <sub>s</sub> P <sub>AR</sub> 112 SmAP <sub>R</sub> 143 Iso [30.2] [2.4] [-] [4.6]
<b>3F12</b>	12	Cr 104 (SmC <sub>a</sub> P <sub>A</sub> 98) SmC <sub>s</sub> P <sub>A</sub> 108 SmC <sub>s</sub> P <sub>AR</sub> ~111 SmC <sub>s</sub> P <sub>R</sub> <sup>[*]</sup> 135 SmA 147 Iso [27.3] [-] [1.1] [-] [-] [5.5]
<b>3F14</b>	14	Cr 101 (SmC <sub>a</sub> P <sub>A</sub> 98) SmC <sub>s</sub> P <sub>A</sub> 107 SmC <sub>s</sub> P <sub>AR</sub> ~112 SmC <sub>s</sub> P <sub>R</sub> <sup>[*]</sup> 134 SmC <sub>s</sub> <sup>[*]</sup> 142 SmA 147 Iso [36.0] [-] [0.9] [-] [-] [0.2] [6.2]
<b>3F16</b>	16	Cr 101 (SmC <sub>a</sub> P <sub>A</sub> 93) SmC <sub>s</sub> P <sub>A</sub> 105 SmC <sub>s</sub> P <sub>AR</sub> ~112 SmC <sub>s</sub> P <sub>R</sub> <sup>[*]</sup> 126 SmC <sub>s</sub> <sup>[*]</sup> 145 SmA 149 Iso [32.3] [-] [0.8] [-] [-] [0.2] [5.7]
<b>3F18</b>	18	Cr 102 (SmC <sub>a</sub> P <sub>A</sub> 94 SmC <sub>s</sub> P <sub>A</sub> 101) SmC <sub>s</sub> P <sub>AR</sub> ~108 SmC <sub>s</sub> P <sub>R</sub> <sup>[*]</sup> 121 SmC <sub>s</sub> <sup>[*]</sup> 143 SmA 148 Iso [57.1] [-] [0.9] [-] [-] [0.3] [6.1]
<b>3F20</b>	20	Cr 104 (SmC <sub>a</sub> P <sub>A</sub> 92 SmC <sub>s</sub> P <sub>A</sub> 98) SmC <sub>s</sub> P <sub>AR</sub> ~110 SmC <sub>s</sub> <sup>[*]</sup> 141 SmA 145 Iso [57.1] [-] [0.9] [-] [0.3] [5.6]

<sup>a</sup>Transition temperatures and enthalpy values (in square brackets) were taken from the second DSC heating scans (10 K min<sup>-1</sup>); transitions without detectable DSC peak were determined by polarizing microscopy without applied field, the SmAP<sub>R</sub>-SmAP<sub>AR</sub> and SmC<sub>s</sub>P<sub>AR</sub>-SmC<sub>s</sub><sup>[\*]</sup>-SmC<sub>s</sub>P<sub>R</sub><sup>[\*]</sup> transition temperatures were determined by investigations under a triangular wave field of 27 V<sub>pp</sub>μm<sup>-1</sup> in all cases; values between brackets are monotropic phase transitions and in this case the enthalpy values were taken on cooling. Abbreviations: Cr = crystalline solid; Iso = isotropic liquid; N<sub>cybA</sub> = nematic phase with cybotactic clusters of the SmA-type; SmA = uniaxial smectic phase; SmAP<sub>R</sub> = high permittivity paraelectric SmA phase showing one broad polarization current peak per half period of an applied E-field; SmAP<sub>AR</sub> = uniaxial (tilt randomized) high permittivity tilt randomized paraelectric SmC phase showing two polarization current peaks per half period of an applied E-field; SmC<sub>s</sub><sup>[\*]</sup> = synclitic tilted (biaxial) smectic C phase (SmC<sub>s</sub>) capable of surface induced mirror symmetry breaking (<sup>[\*]</sup>); SmC<sub>s</sub>P<sub>R</sub><sup>[\*]</sup> = high permittivity range of the paraelectric SmC<sub>s</sub> phase showing one broad polarization current peak per half period of an applied E-field; SmC<sub>s</sub>P<sub>AR</sub> = high permittivity paraelectric range of the SmC<sub>s</sub><sup>[\*]</sup> phase showing two polarization current peaks per half period of an applied E-field; SmC<sub>s</sub>P<sub>A</sub> = antiferroelectric switching polar and synclitic tilted SmC<sub>s</sub> phase; SmC<sub>a</sub>P<sub>A</sub> = antiferroelectric switching polar anticlinic tilted SmC phase; see also Figure 1b. For selected DSCs, see Figure S6; data of **3F20** were taken from ref.<sup>[37]</sup> and phase notation was adjusted to the rules used herein.

**Table 2.** Effect of different 3-substituents on the LC phases and polar order.<sup>a</sup>

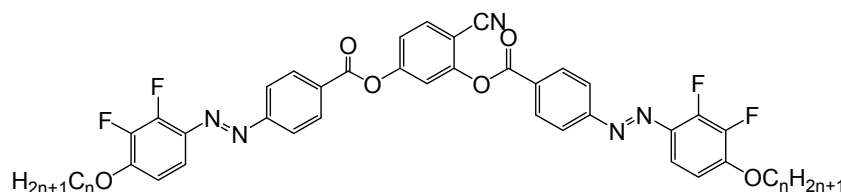
Comp.	X	$T/^{\circ}\text{C}$ [ $\Delta H/\text{kJ}\cdot\text{mol}^{-1}$ ]
<b>H18</b>	H	Cr 80 (SmC <sub>s</sub> P <sub>A</sub> 76 M <sub>1</sub> 79) SmC <sub>s</sub> P <sub>AR</sub> ~98 SmC <sub>s</sub> P <sub>R</sub> <sup>[*]</sup> ~116 SmC <sub>s</sub> <sup>[*]</sup> 142 Iso <sup>[32b]</sup>
<b>3F18</b>	F	Cr 102 (SmC <sub>a</sub> P <sub>A</sub> 94 SmC <sub>s</sub> P <sub>A</sub> 101) SmC <sub>s</sub> P <sub>AR</sub> ~108 SmC <sub>s</sub> P <sub>R</sub> <sup>[*]</sup> 121 SmC <sub>s</sub> <sup>[*]</sup> 143 SmA 148 Iso
<b>3Br18</b>	Br	Cr 86 (SmC <sub>s</sub> P <sub>AR</sub> 82) SmC <sub>s</sub> <sup>[*]</sup> 108 SmA 117 Iso [23.4] [-] [0.2] [3.7]
<b>3Me18</b>	CH <sub>3</sub>	Cr 79 SmC 90 N <sub>Cybc</sub> <sup>b</sup> 92 Iso [69.9] [0.8] [1.8]

<sup>a</sup> Abbreviations are explained in Table 1; <sup>b</sup>based on the presence of the SmC low temperature phase the nematic phase is designated as N<sub>Cybc</sub>.

**Table 3.** Phase transitions of compounds **2Fn** with 2-fluorination.<sup>a</sup>

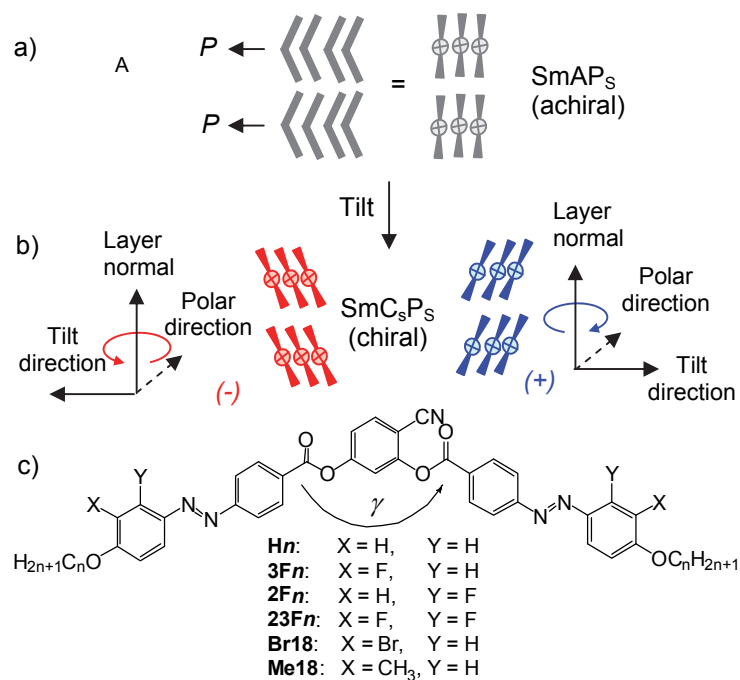
Comp.	<i>n</i>	$T/^{\circ}\text{C}$ [ $\Delta H/\text{kJ}\cdot\text{mol}^{-1}$ ]
<b>2F8</b>	8	Cr 107 N <sub>Cybc</sub> 117 Iso [43.0] [0.7]
<b>2F10</b>	10	Cr 86 N <sub>Cybc</sub> 100 Iso [40.8] [0.9]
<b>2F12</b>	12	Cr 92 (SmC 69) N <sub>Cybc</sub> 112 Iso [43.5] [0.3] [0.9]
<b>2F14</b>	14	Cr 91 (SmC 91) N <sub>Cybc</sub> 104 Iso [40.1] [0.9] [1.4]
<b>2F16</b>	16	Cr 92 SmC 102 N <sub>Cybc</sub> 108 Iso [50.7] [0.9] [1.7]

<sup>a</sup>Transition temperatures and enthalpy values (in square brackets) were taken from the second DSC heating scans (10 K min<sup>-1</sup>); values between brackets are monotropic phase transitions and in this case the enthalpy values are taken from the first DSC cooling scans; for abbreviations see Table 1 and Figure 11.

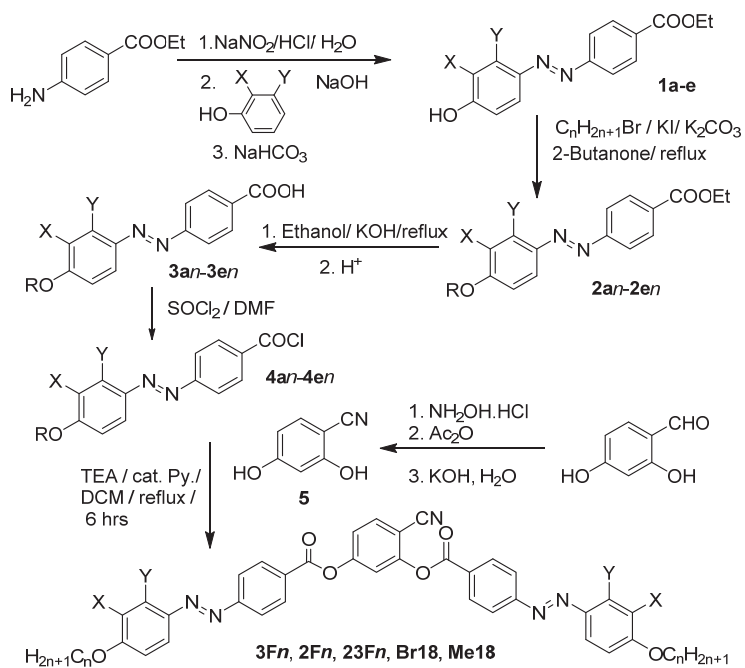
**Table 4.** Phase transitions of series of 2,3-difluorinated compounds **23Fn**.<sup>a</sup>

Comp.	<i>n</i>	<i>T</i> /°C	
		[Δ <i>H</i> /kJ·mol <sup>-1</sup> ]	
<b>23F8</b>	8	Cr 133 Iso	[28.7]
<b>23F10</b>	10	Cr 131 (SmA 129) Iso	[39.3] [3.5]
<b>23F12</b>	12	Cr 126 SmC <sub>s</sub> <sup>[*]</sup> 134 Iso	[36.9] [4.9]
<b>23F14</b>	14	Cr <sub>1</sub> 71 Cr <sub>2</sub> 122 SmC <sub>s</sub> <sup>[*]</sup> 136 Iso	[22.9] [37.8] [5.9]
<b>23F16</b>	16	Cr <sub>1</sub> 83 Cr <sub>2</sub> 123 SmC <sub>s</sub> <sup>[*]</sup> 140 Iao	[26.2] [36.1] [6.4]

<sup>a</sup>Transition temperatures and enthalpy values (in square brackets) were taken from the second DSC heating scans (10 K min<sup>-1</sup>); values between brackets are monotropic phase transitions and in this case the enthalpy values are taken from the first DSC cooling scans; for abbreviations see Table 1.



Scheme 1



Scheme 2

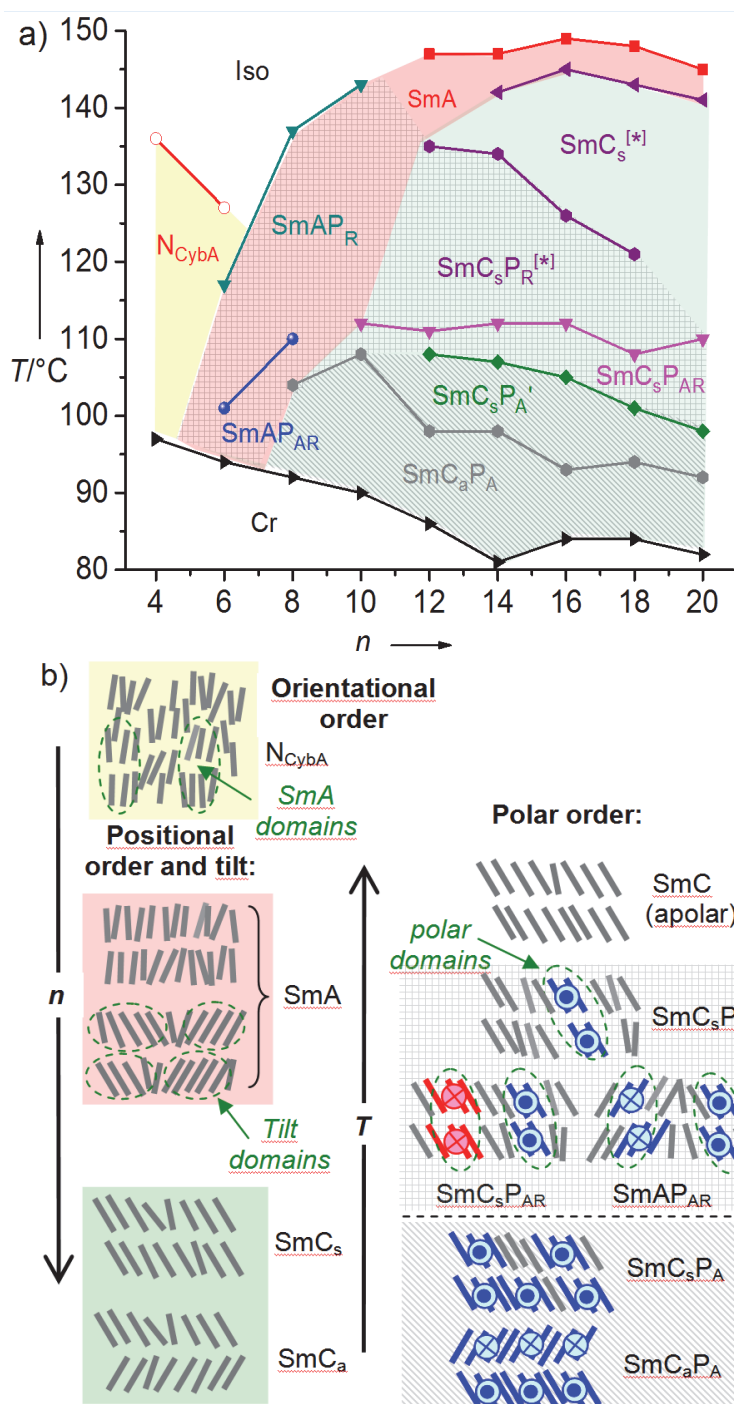


Figure 1

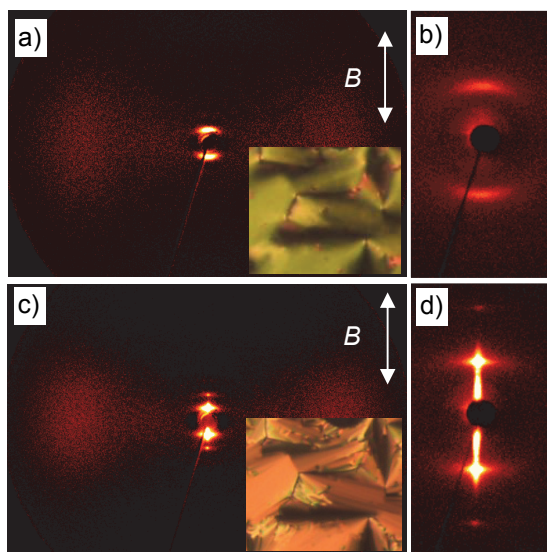


Figure 2.

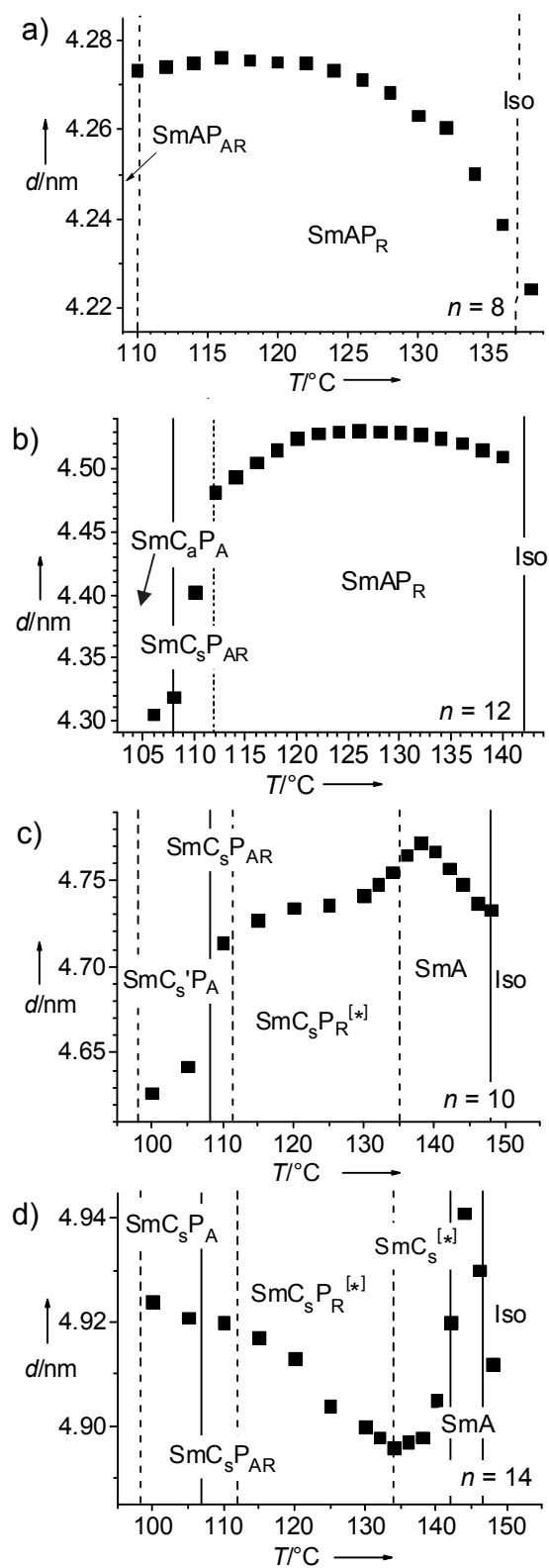


Figure 3.

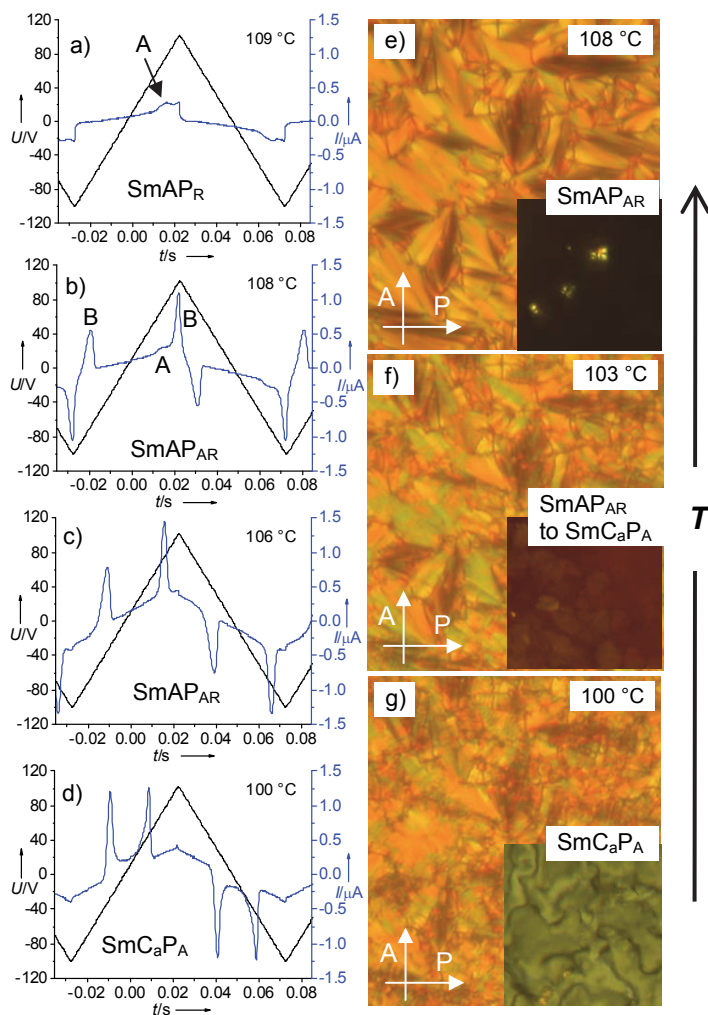


Figure 4

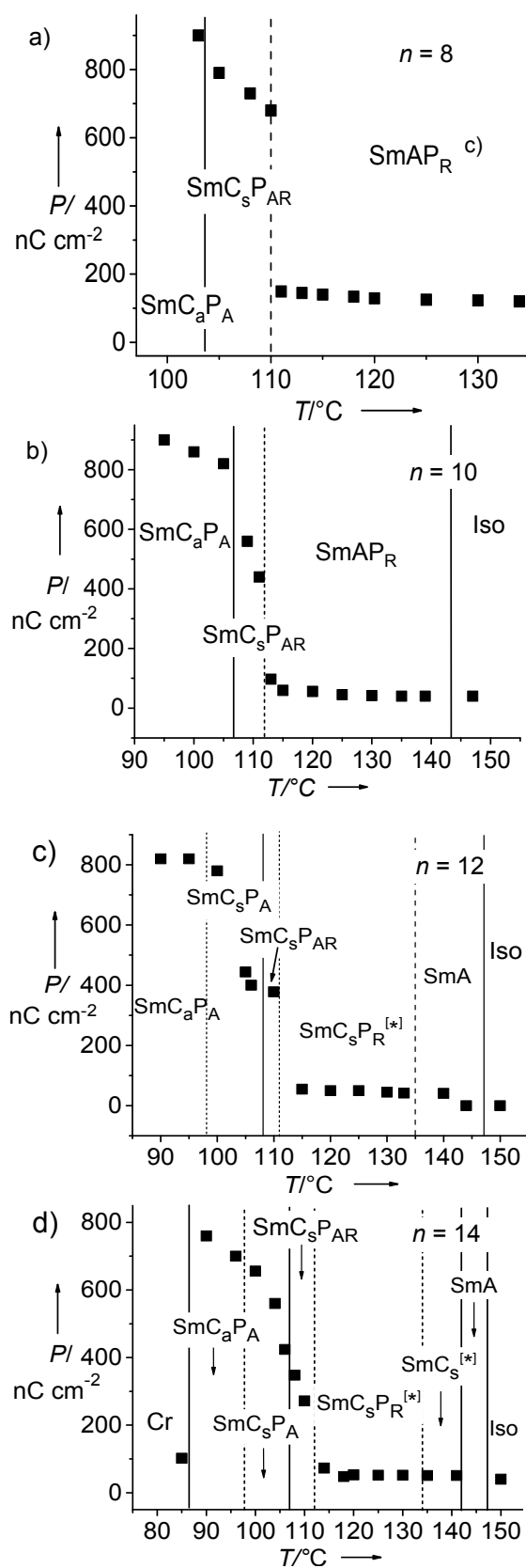


Figure 5.

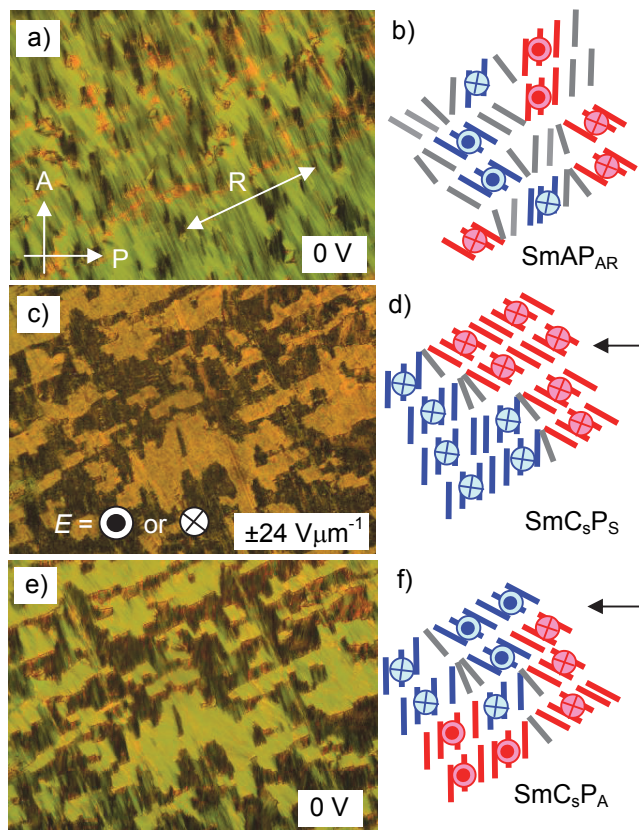


Figure 6.

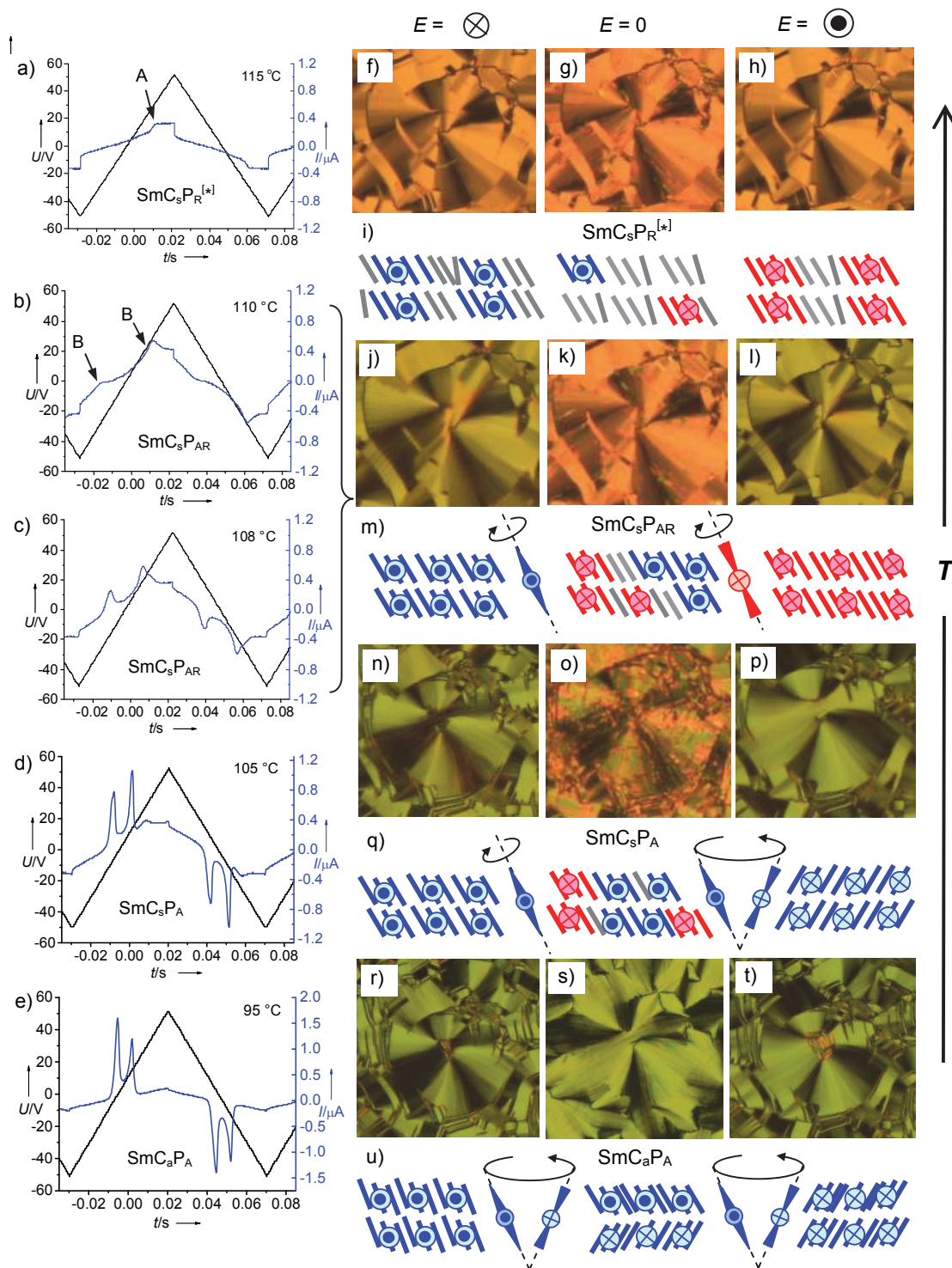


Figure 7.

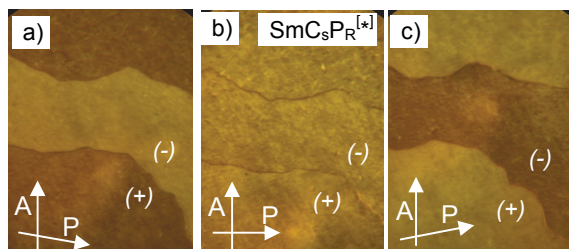


Figure 8.

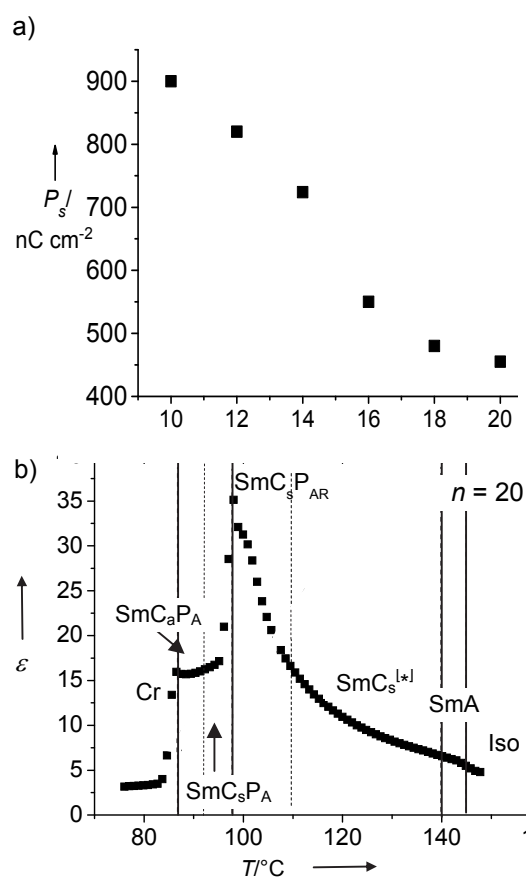


Figure 9.

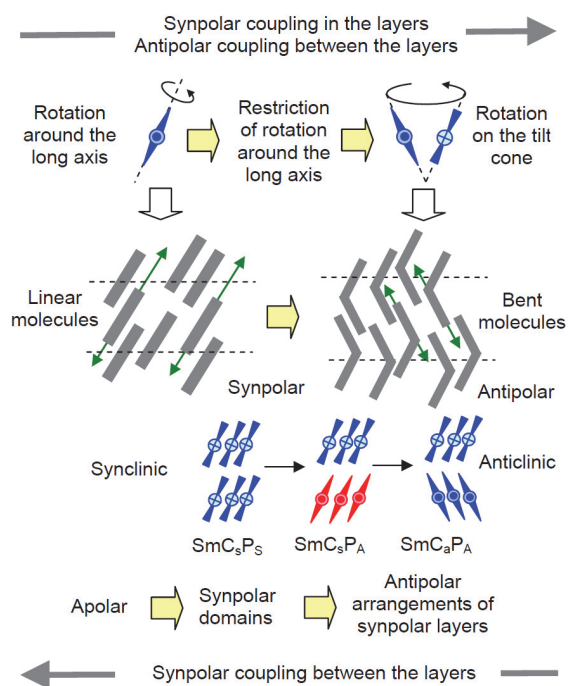


Figure 10.

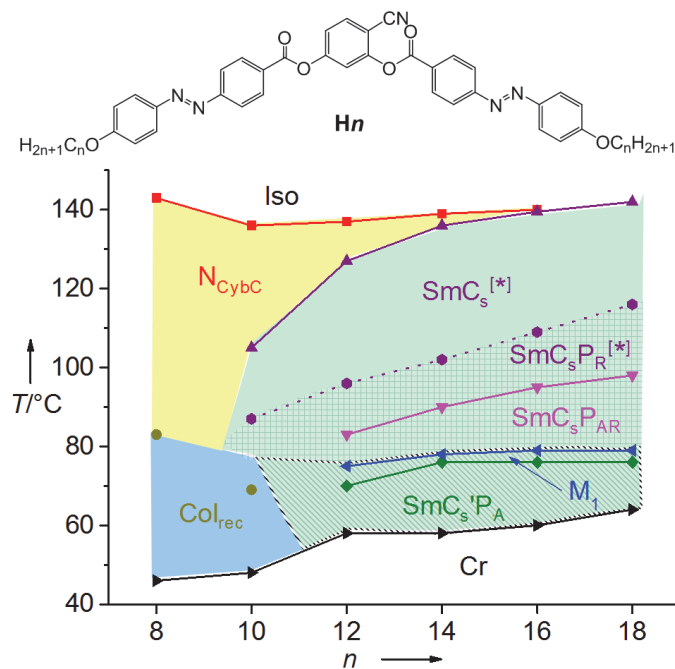
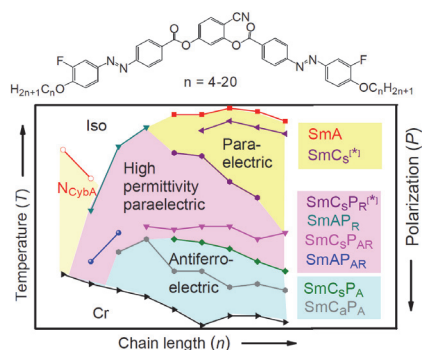


Figure 11.

## Graphical abstract



**Soft organic ferroelectrics.** The shown liquid crystalline compounds show a paraelectric-ferroelectric transition by gradual increase of the size of polar domains and crossing a permittivity maximum, similar to inorganic solid state ferroelectrics.

**Keywords:** Bent-core liquid crystals; ferroelectricity; azobenzene; mirror symmetry breaking; fluorine substitution